Structural Safety 112 (2025) 102545

Contents lists available at ScienceDirect

Structural Safety

journal homepage: www.elsevier.com/locate/strusafe

A novel deterministic sampling approach for the reliability analysis of high-dimensional structures

Yang Zhang [a,d], Jun Xu [a,b,*], Enrico Zio [c,d]

[a] College of Civil Engineering, Hunan University, Changsha, 410082, PR China
[b] State Key Laboratory of Bridge Engineering Safety and Resilience, Hunan University, 410082, PR China
[c] Centre for Research on Risk and Crises (CRC), Mine Paris-PSL University, Rue Claude Daunesse 1, 06904 Sophia Antipolis, France
[d] Energy Department, Politecnico di Milano, Via La Masa 34, Milano 20156, Italy

ARTICLE INFO

Keywords:
High-dimensional reliability analysis
Number-theoretical method
Cutting method
Generating vector
Maximum entropy method
Box–Cox transformation

ABSTRACT

Overcoming the "curse of dimensionality" in high-dimensional reliability analysis is still an enduring challenge. This paper proposes an innovative deterministic sampling method designed to overcome this challenge. The approach starts with a two-dimensional uniform point set, generated using the good lattice point method. This set is then refined through the cutting method to produce a specific number of points. A novel generating vector is computed based on this method, enabling the generation of the targeted high-dimensional point set through a strategic dimension-by-dimension mapping. Notably, this method eliminates the need for complex congruence computation and primitive root optimization, enhancing its efficiency for high-dimensional sampling. The resulting point set is deterministic and uniform, greatly reducing variability in reliability analysis. Then, the proposed approach is integrated into the fractional exponential moment-based maximum entropy method with the Box–Cox transform. This integration efficiently recovers the probability distribution for the limit state function (LSF) with high-dimensional inputs, enabling precise assessment of the failure probability. The efficacy of the proposed method is demonstrated through three high-dimensional numerical examples, involving both explicit and implicit LSFs, highlighting its applicability for high-dimensional reliability analysis of structures.

1. Introduction

The inherent uncertainties in practical engineering systems, such as randomness in geometrical configurations, material properties, boundary conditions, and loading conditions [1], underscore the importance of reliability analysis in high-dimensional structures. The complexity of this task is compounded by the need to express failure probabilities as multiple integrals within the failure domain [2,3], a process complicated by the intricate topology of the limit state surface [4]. Addressing these challenges, a spectrum of approximate methods for reliability analysis has evolved, falling into four primary categories: approximate analytical methods, sampling methods, surrogate model-based methods, and numerical integration methods. These methodologies are instrumental in navigating the complexities of structural reliability assessment amidst the pervasive uncertainties in engineering systems.

Approximate analytical methods approach reliability by conducting a Taylor series expansion of the Limit State Function (LSF) at the most probable point. Key techniques include the First Order-Reliability Method (FORM) [5,6] and the Second-Order Reliability Method (SORM) [7,8]. These methods, which employ first and second-order Taylor expansions, are efficient and widely utilized [9,10]. However, they may not always be suitable for reliability problems involving high dimensions and structural nonlinearities due to the omission of higher-order information [11–14]. Consequently, the design point and its vicinity become less relevant for estimating failure probabilities in high-dimensional problems [12]. Additionally, approximations of the LSF may not be feasible, as the shape of the failure region can become highly complex due to structural nonlinearities [12]. Sampling methods estimate failure probabilities through extensive model evaluations. Monte Carlo Simulation (MCS), a benchmark in this category, is applicable regardless of the number of random variables involved in the problem or the nature of the structural model (whether linear or nonlinear) [12]. However, MCS faces significant computational challenges, particularly for systems with a small failure probability, as a large number of samples are required to obtain an estimator with sufficient accuracy [11,12]. Enhanced MCS techniques, including Importance Sampling (IS) [15], improved cross-entropy methods [16,17], sequential IS [18], sequential directional IS [19], Subset Simulation (SS) [20,

* Corresponding author at: College of Civil Engineering, Hunan University, Changsha, 410082, PR China.
E-mail addresses: zhangyang98@hnu.edu.cn (Y. Zhang), xujun86@hnu.edu.cn (J. Xu), enrico.zio@polimi.it (E. Zio).

https://doi.org/10.1016/j.strusafe.2024.102545
Received 22 February 2024; Received in revised form 31 October 2024; Accepted 7 November 2024
Available online 20 November 2024
0167-4730/

Nomenclature

CDF	Cumulative Distribution Function
FEM	Fractional Exponential Moment
FM	Fractional Moment
FORM	First-Order Reliability Method
GLP	Good Lattice Points
IS	Importance Sampling
LSF	Limit State Function
MCS	Monte Carlo Simulation
MEM	Maximum Entropy Method
NTM	Number-Theoretical Method
PDF	Probability Distribution Function
SORM	Second-Order Reliability Method
SS	Subset Simulation

21], and line sampling [22,23], etc., have been developed to increase efficiency and have demonstrated robust performance. However, despite these advancements, the accuracy and computational demands of these methods may still remain significant challenges, particularly for costly LSF evaluations involving high-dimensional inputs, nonlinearity, or low failure probabilities [24–26]. Surrogate model-based methods provide computational efficiency by replacing the original LSF with a less computationally expensive mathematical expression derived from training samples. Various techniques have been developed, including response surface methods [27,28], support vector machines [29,30], Kriging methods [31–33], and artificial neural networks [34,35]. Polynomial chaos expansions have also been widely used [36–38]. Despite their success in low-dimensional problems, these methods struggle with the "curse of dimensionality" in high-dimensional scenarios [39–41], leading to prohibitive computational costs for realistic systems and structures. Integration of dimensionality reduction strategies with surrogate models [42–44] has been attempted, yet significant computational demands persist in practices [25]. Numerical integration methods estimate the Probability Density Function (PDF) of the LSF based on statistical moments, followed by one-dimensional integration for reliability analysis [11]. Central to these methods is the accurate estimation of statistical moments and PDF reconstruction. Moment-based reliability analysis methods, such as the Pearson system [45], Generalized Lambda distribution [46], and the Maximum Entropy Method (MEM) [47], have gained prominence. Notably, MEM relies on statistical moments for PDF reconstruction without additional assumptions [48]. Variants of MEM, including integer moment-based MEM [49], Fractional Moment-based MEM (FM-MEM) [50–52], and Fractional Exponential Moment-based MEM (FEM-MEM) [24,53,54], have been developed for efficiency. However, the challenge in these methods lies in the selection of the point set for statistical moment estimation, which significantly affects the accuracy of the reliability analysis. Despite the significant contributions of these methods to reliability assessment, balancing accuracy and efficiency in high-dimensional problems remains a formidable challenge. The intricate interplay of computational demands and the need for precision in reliability analysis continues to drive research in this field.

To address the aforementioned limitations and achieve a balance between accuracy and efficiency in high-dimensional reliability analysis of structures, this paper proposes a novel deterministic sampling method in the framework of FEM-MEM. In the proposed method, two strategies, i.e., a cutting strategy and a two-round sorting strategy, are implemented to generate a high-dimensional uniform point set for LSF moments assessment. Then, the FEM-MEM combined with the Box–Cox transformation is applied to reconstruct the PDF of LSF. The proposed method can effectively calculate the failure probability and reliability index of structures with high-dimensional inputs.

The structure of this paper is organized as follows: Section 2 presents a concise overview of the Number-Theoretical Method (NTM), including Good Lattice Point (GLP) (Section 2.1) and an improved GLP with dimension-by-dimension mapping strategy (DD-GLP) (Section 2.2). In Section 3, the proposed high-dimensional deterministic sampling approach is introduced, based on a cutting method (Section 3.1) and a generating vector construction strategy (Section 3.2). Section 4 considers the high-dimensional reliability problem (Section 4.1), and outlines a probability reconstruction method based on the Box–Cox transformation (Section 4.2) and FEM-MEM (Section 4.3). A step-by-step description of the implementation of the proposed method is provided in Section 5. Three numerical examples are presented in Section 6 to illustrate the performance and effectiveness of the proposed method. Finally, Section 7 contains the concluding remarks.

2. Overview of NTM-based sampling methods

As the introduction highlights, conventional methods often prove inefficient when confronted with high-dimensional problems. Therefore, this paper proposes a novel sampling method combined with FEM-MEM to address the challenges posed by high-dimensional reliability analysis problems. Generally, a uniform point set with low discrepancy is advantageous for moment estimation and reliability analysis [24,55,56]. Notably, a specific category of NTM points, called GLP point set [57,58], is tailored to minimize discrepancies for uniform design [59]. Given the desirable space-filling property of the GLP-generated uniform point set [55], GLP points find widespread application in enhancing accuracy and minimizing errors in the reliability analysis of structures. In that regard, to ensure accuracy in the FEMs assessment, the high-dimensional uniform sampling method is constructed in this paper, relying on the GLP and DD-GLP method [60]. To provide context, the fundamentals of GLP and DD-GLP are briefly revisited in this section. The properties of these two methods will also be identified and discussed, serving as motivation for the proposed sampling method described in Section 3.

2.1. GLP

In the GLP method, the construction of the generating vector $\mathbf{h}$ is the initial step to generate a uniform point set $\mathcal{P}_\theta = \left\{\theta_q = \left(\theta_q^{(1)}, \theta_q^{(2)}, \ldots, \theta_q^{(d)}\right),\ q = 1, 2, \ldots, n\right\}$ with n points within the relevant unit hypercube space $C^d = [0,1]^d$, which can be achieved by [57,58]

$$\mathbf{h} = (h_1, h_2, \ldots, h_i, \ldots, h_d) \equiv \left(1, a, a^2, \ldots, a^{i-1}, \ldots, a^{d-1}\right) (\bmod n),\ \ i = 1, 2, \ldots, d \tag{1}$$

where a is the primitive root of the prime number n, i.e., $a_{i'} (\bmod\ n) \neq a_{j'} (\bmod\ n)$, $(1 \le i' < j' < n)$, $1 < h_i < n$ $(h_i \neq h_j,\ i \neq j; i, j = 1, 2, \ldots, d)$, the integers h_i and a^{i-1} are congruent modulo n, $(\bmod\ n)$ denoted as the congruence theorem, and n stands for the number of points.

Then, the q-th component in the i-th dimension of the GLP point set $\theta_q^{(i)}$ in the unit hypercube space $C^d = [0,1]^d$ can be determined using the formula below [57,58]

$$\begin{cases} Q_q^{(i)} \equiv q h_i (\bmod\ n) \\ \theta_q^{(i)} = (2Q_q^{(i)} - 1)/2n \end{cases} \quad q = 1, 2, \ldots, n; i = 1, 2, \ldots, d \tag{2}$$

where the integers $Q_q^{(i)}$ and $q h_i$ are congruent modulo n, with $1 \le Q_q^{(i)} \le n$.

According to the properties of the congruence theorem, Eq. (2) can be further expressed as

$$\theta_q^{(i)} = \frac{2qh_i - 1}{2n} - \mathrm{int}\left(\frac{2qh_i - 1}{2n}\right) = \mathrm{dec}\left(\frac{2qh_i - 1}{2n}\right) \tag{3}$$

where $\mathrm{int}(\cdot)$ represents a mathematical operation to obtain the integer part of a real number, whereas $\mathrm{dec}(\cdot)$ denotes the decimal part.

2.2. DD-GLP

Although the GLP method [57,58] (Section 2.1) can generate uniform points with low discrepancy in a straightforward manner, it encounters a NP-hard problem when computing the essential generating vector $\mathbf{h}$ in Eq. (1) in a high-dimensional random-variate space [60]. This leads to an unacceptable computational burden, potentially causing the failure to generate the point set $\mathcal{P}_{\theta}$. To overcome this issue, Gao et al. [60] proposed the DD-GLP method, which enhances the efficiency of constructing the generating vector and point set in a high-dimensional random-variate space.

In contrast to the traditional GLP method (Section 2.1), which requires exponent calculation to form the generating vector Eq. (1), the DD-GLP method constructs the generating vector with its components expressed as linear multiples of the primitive root a of the prime number n, as follows [60]

$$\begin{cases} \mathbf{e} = (e_1, e_2, \dots, e_q, \dots, e_n) \equiv (a, 2a, \dots, qa, \dots, na)(\mathrm{mod}\, n) \\ 0 < e_q \leq n \end{cases}, q = 1, 2, 3, \dots, n \tag{4}$$

where the integers e_q and qa are congruent modulo n.

Then, the uniform point set $\mathcal{P}_{\theta}$ in the unit hypercube space $C^d = [0,1]^d$ can be generated by the DD-GLP as follows [60]

$$\begin{cases} e_q \equiv qa(\mathrm{mod}\, n) \\ \theta_q^{(i)} = \theta_{e_q}^{(i-1)}, q = 1, 2, 3, \dots, n; i = 1, 2, 3, \dots, d \end{cases} \tag{5}$$

The selection of an appropriate primitive root a is crucial for generating a point set with good uniformity. The optimal primitive root a can be determined by satisfying the following equation, as follows [61]

$$D_n\left(\mathcal{P}_{\theta}\right) \leq \frac{d}{n} + \frac{1}{2n}(0.81 + 2\log n)^d \tag{6}$$

where $D_n\left(\mathcal{P}_{\theta}\right)$ represents the star discrepancy of the point set generated by the primitive root a, defined as [57]

$$D_n\left(\mathcal{P}_{\theta}\right) = \sup_{[\boldsymbol{l},\boldsymbol{r}) \in C^d} \left| \frac{n_{\mathrm{sel}}\left([\boldsymbol{l},\boldsymbol{r}), \mathcal{P}_{\theta}\right)}{n} - V([\boldsymbol{l},\boldsymbol{r})) \right| \tag{7}$$

where $n_{\mathrm{sel}}\left([\boldsymbol{l},\boldsymbol{r}), \mathcal{P}_{\theta}\right)$ is the number of points in $\mathcal{P}_{\theta}$ that satisfy $\theta_q \in [\boldsymbol{l},\boldsymbol{r})$, $0 \leq \boldsymbol{l} \leq \boldsymbol{r} \leq 1$, and $V([\boldsymbol{l},\boldsymbol{r})) = \prod_{i=1}^{d}\left(l_i, r_i\right)$ represents the volume of $[\boldsymbol{l},\boldsymbol{r})$.

Eq. (5) illustrates that the DD-GLP method conveniently generates a low-discrepancy uniform point set using the dimension-by-dimension mapping strategy, leading to an easily implementable recursive relationship. However, this approach still necessitates a large number of samples ($n > 10^5$ points for $d > 100$) in high-dimensional random sample space to ensure the uniformity of the point set [60], as the discrepancy limit is constrained by the right-hand side of inequality (6). Moreover, the computationally intensive congruence computation and primitive root optimization processes for a large number n are still inevitably present in the DD-GLP method, rendering it impractical for direct application in engineering practice. It is worth highlighting that both the GLP and DD-GLP generate deterministic point sets, which show no variabilities.

3. A novel high-dimensional deterministic sampling method

Considering the limitations of the DD-GLP method, a novel high-dimensional deterministic sampling method, based on GLP and incorporating a cutting strategy along with a new strategy for deriving the generating vector, is proposed. This method aims to generate a low-discrepancy uniform point set, ensuring the accuracy of high-dimensional reliability analysis of structures with a smaller sample size. In this method, the cutting strategy [62] is employed both to obtain the position information of points within the GLP point set as the basis for constructing the generating vector and to reduce the number of points required in reliability analysis while ensuring accuracy. Simultaneously, the proposed generating vector construction strategy is developed to extract the position information of points within the uniform point set obtained through the cutting strategy, thereby facilitating the elegant construction of a new generating vector while achieving the goal of circumventing the computationally intensive congruence computation and primitive root optimization processes. The details of the proposed method will be elaborated in this section.

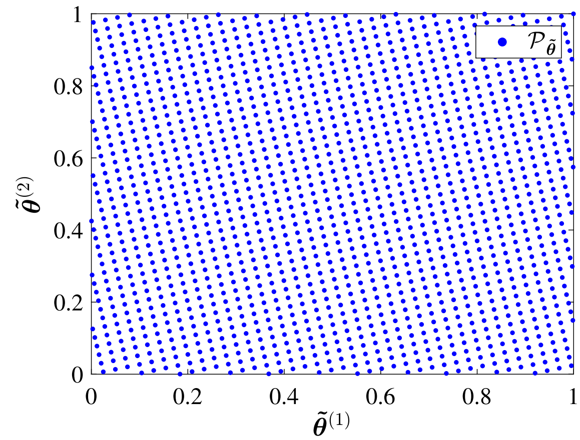

Fig. 1. Schematic of the initial two-dimensional GLP point set $\mathcal{P}_{\tilde{\theta}}$.

3.1. Cutting strategy

To address the requirement for a large number of points, a cutting strategy [62] is first proposed to obtain a two-dimensional cutting point set $\mathcal{P}_{\boldsymbol{u}} = \left\{\boldsymbol{u}_{\bar{q}} = \left(u_{\bar{q}}^{(1)}, u_{\bar{q}}^{(2)}\right), \bar{q} = 1, 2, \dots, n_t\right\}$ with an arbitrary target number of points n_t, where $n_t < n$. This target number is significantly smaller than the number of points n in the initial DD-GLP point set $\mathcal{P}_{\theta}$. It is important to note that the proposed method only requires cutting the first two dimensions of the point set $\mathcal{P}_{\theta}$ using the cutting strategy. In other words, the proposed method does not need to generate the complete DD-GLP point set $\mathcal{P}_{\theta}$ containing all dimensions, thereby saving computational efforts compared to the DD-GLP method.

In this context, to obtain a two-dimensional cutting point set $\mathcal{P}_{\boldsymbol{u}}$, the initial two-dimensional GLP point set $\mathcal{P}_{\tilde{\theta}} = \left\{\tilde{\theta}_q = \left(\tilde{\theta}_q^{(1)}, \tilde{\theta}_q^{(2)}\right), q = 1, 2, \dots, n\right\}$ needs to be determined using Eq. (2) or Eq. (5). In this paper, the number of points in the point set $\mathcal{P}_{\tilde{\theta}}$ is chosen to be $n = 1597$, and the primitive root is set to $a = 679$ in accordance with Eq. (6). Then, the points of $\mathcal{P}_{\tilde{\theta}}$ can be calculated as depicted in Fig. 1.

The cutting strategy is, then, implemented by cutting the two-dimensional initial point set $\mathcal{P}_{\tilde{\theta}}$ within the unit square $C^2 = [0,1]^2$ using a square cutting region $C_{\mathrm{cut}}^2 = \left[0, u_{\mathrm{cut}}\right]^2$, $u_{\mathrm{cut}} \in [0,1]$, with side length u_{cut} and one vertex at the origin. The points $\tilde{\theta}_q$s falling within the square cutting region C_{cut}^2 are selected as $\boldsymbol{u}_{\bar{q}}$. To obtain the cutting point set $\mathcal{P}_{\boldsymbol{u}}$, the value of u_{cut} is continuously increased until the number $\bar{n}$ of points falling in the square cutting region C_{cut}^2 reaches the target number n_t. This process is performed iteratively. Once the iteration stopping condition is met, all the points located in the C_{cut}^2 form the cutting point set $\mathcal{P}_{\boldsymbol{u}}$ accordingly. The algorithm for the cutting method is presented in Table 1, and the schematic is shown in Fig. 2. It is important to note that this iterative process does not involve deterministic structural calculations, resulting in no additional computational efforts.

Table 1
Details of the cutting method.

Algorithm 1: Cutting method [62]

1: **while** $\bar{n} < n_t$
  Increase the value of u_{cut};
  $$\mathcal{P}_{\boldsymbol{u}} = \left\{ \tilde{\theta}_q \in \tilde{\theta} : \ \tilde{\theta}_q^{(1)} < u_{\text{cut}} \cap \tilde{\theta}_q^{(2)} < u_{\text{cut}} \ , q = 1, 2, \ldots, n \right\} = \left\{ \boldsymbol{u}_{\bar{q}} = \left(u_{\bar{q}}^{(1)}, u_{\bar{q}}^{(2)} \right), \ \bar{q} = 1, 2, \ldots, \bar{n} \right\};$$
end

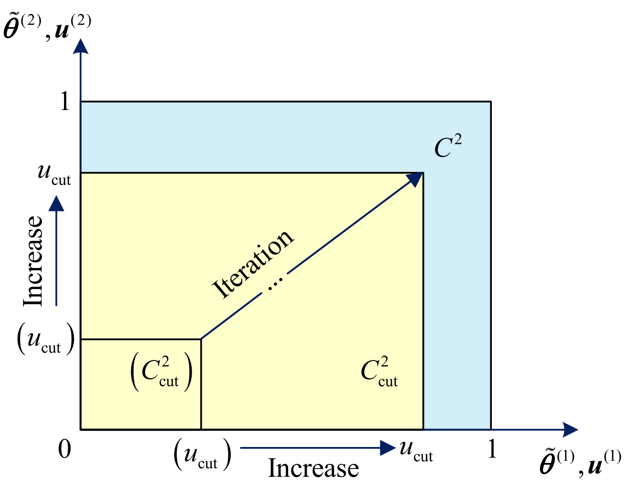

Fig. 2. Schematic of the cutting method.

Since the cutting point set $\mathcal{P}_{\boldsymbol{u}}$ preserves the arrangement of points from the initial two-dimensional GLP point set $\mathcal{P}_{\tilde{\theta}}$, the positional information of this uniform point set is retained [62]. Leveraging this property, a new generating vector for producing a low-discrepancy uniform point set across the entire unit hypercube space, $C^d = [0,1]^d$, can be derived using the method introduced in the next section (Section 3.2).

3.2. A new way to construct the generating vector

The computation of generating vectors is a key and challenging aspect of the GLP method. As mentioned earlier (Section 2.2), traditional GLP methods [57,58] struggle to generate point sets in high-dimensional spaces because the computation of high-dimensional generating vectors is a NP-hard problem. While the DD-GLP method [60] represents an improvement by requiring only linear computation for the generation vector, it still involves prime root optimization and congruence computation for high-dimensional point sets with a large number of points, resulting in significant computational efforts when dealing with high-dimensional problems. The generating vector, essentially a uniform design, determines the arrangement of points in a unit hypercube $C^d = [0,1]^d$ according to the NTM [57]. Moreover, there exists a recursive relationship between different dimensions of the GLP point set Eq. (5), indicating that the position information (or generating vector) of the entire point set can be inferred from the points in any two dimensions. In light of this, this paper proposes a novel method, named the two-round sorting strategy, to construct the generating vector for high-dimensional sampling with high efficiency, detailed in this section.

In the GLP method, the $h_1 = 1$ can always be assumed for $\mathbf{h} = \left(h_1, h_2, \ldots, h_d\right)$ [57]. Accordingly, the values of points of the first-dimension can be expressed using Eq. (3) as:

$$\boldsymbol{\theta}^{(1)} = \left(\theta_1^{(1)}, \theta_2^{(1)}, \ldots, \theta_q^{(1)}, \ldots, \theta_n^{(1)}\right)^T = \left(\frac{1}{2n}, \frac{3}{2n}, \ldots, \frac{2q-1}{2n}, \ldots, \frac{2n-1}{2n}\right)^T, q = 1, 2, \ldots, n \tag{8}$$

Clearly, the points in the first dimension of the GLP point set are arranged in ascending order on $[0,1]$. Moreover, according to DD-GLP, the points in the second dimension can be generated recursively by the points in the first dimension based on the generation vector Eq. (5). Therefore, the generation vector not only determines the arrangement but also the numerical order of the points in the second dimension. In other words, the numerical order of the points on the second dimension of the cutting point set $\mathcal{P}_{\boldsymbol{u}}$ can be used to derive the generating vector, which is the core of the proposed method.

For ease of understanding, let us consider an example with $d = 3$, $n = 7$, and the primitive root $a = 3$ of the prime number 7. According to Eq. (1), the generating vector $\mathbf{h}$ of the GLP algorithm can be expressed as:

$$\mathbf{h} = \left(h_1, h_2, h_3\right) = (1, 3, 2) \tag{9}$$

The generating vector $\mathbf{e}$ of the DD-GLP algorithm can be obtained via Eq. (4) as:

$$\mathbf{e} = \left(e_1, e_2, \ldots, e_7\right) = (3, 6, 2, 5, 1, 4, 7) \tag{10}$$

Values of the first two-dimension points of the point set can be obtained from Eq. (2) or Eq. (3) as

$$\begin{aligned}
\boldsymbol{\theta} = \left[\boldsymbol{\theta}^{(1)} \quad \boldsymbol{\theta}^{(2)}\right] &= \begin{pmatrix} \theta_1^{(1)} & \theta_2^{(1)} & \theta_3^{(1)} & \theta_4^{(1)} & \theta_5^{(1)} & \theta_6^{(1)} & \theta_7^{(1)} \\ \theta_1^{(2)} & \theta_2^{(2)} & \theta_3^{(2)} & \theta_4^{(2)} & \theta_5^{(2)} & \theta_6^{(2)} & \theta_7^{(2)} \end{pmatrix}^T \\
&= \begin{pmatrix} \theta_1^{(1)} & \theta_2^{(1)} & \theta_3^{(1)} & \theta_4^{(1)} & \theta_5^{(1)} & \theta_6^{(1)} & \theta_7^{(1)} \\ \theta_3^{(1)} & \theta_6^{(1)} & \theta_2^{(1)} & \theta_5^{(1)} & \theta_1^{(1)} & \theta_4^{(1)} & \theta_7^{(1)} \end{pmatrix}^T \\
&= \begin{pmatrix} 1/14 & 3/14 & 5/14 & 7/14 & 9/14 & 11/14 & 13/14 \\ 5/14 & 11/14 & 3/14 & 9/14 & 1/14 & 7/14 & 13/14 \end{pmatrix}^T
\end{aligned} \tag{11}$$

It can be noticed that in Eq. (11), the generating vector determines the numerical order of the points on the second dimension of the point set. For clarity, the schematic diagram is shown in Fig. 3.

Since one of the vertices of the square cutting region $C^2_{\text{cut}} = \left[0, u_{\text{cut}}\right]^2$ is at the coordinate origin, as shown in Fig. 4, the points of the first dimension of the cutting point set $\mathcal{P}_{\boldsymbol{u}}$ also form an ascending series on the interval $[0, u_{\text{cut}}]$. Additionally, the cutting process does not change the original arrangement of the GLP point set. Therefore, the numerical order of points on the second dimension of the cutting point set $\mathcal{P}_{\boldsymbol{u}}$ contains the full information of the generating vector of $\mathcal{P}_{\boldsymbol{u}}$, as shown in Fig. 5. In that regard, once the cutting point set $\mathcal{P}_{\boldsymbol{u}}$ is obtained by the cutting strategy (Section 3.1), the task is transformed to determining the numerical order $\mathbf{v} = \left(v_1, v_2, \ldots, v_{\bar{q}}, \ldots, v_{n_t}\right)$, $\bar{q} = 1, 2, \ldots, n_t$, of the points on the second dimension of the cutting point set $\mathcal{P}_{\boldsymbol{u}}$. To achieve this, a two-round sorting strategy is proposed to calculate the numerical order $\mathbf{v}$.

In the first-round sorting operation, the task is to sort the second dimension of the cutting point set, denoted as $\boldsymbol{u}^{(2)}$, resulting in the sorted set $\bar{\boldsymbol{u}} = \left(\bar{u}_1, \bar{u}_2, \ldots, \bar{u}_{\bar{q}}, \ldots, \bar{u}_{n_t}\right)$. Additionally, it is necessary to calculate the corresponding position vector, denoted as $\mathscr{P}_{\bar{\boldsymbol{u}}}$, representing the positions of the sorted elements $\bar{u}_{\bar{q}}$s in $\boldsymbol{u}^{(2)}$. It is evident that each element $u_{\bar{q}}^{(2)}$ in the set $\boldsymbol{u}^{(2)}$ has a one-to-one correspondence with the position vector of $\boldsymbol{u}^{(2)}$, defined as $\mathscr{P} = \left[1, 2, \ldots, n_t\right]$, which consists of the positions of each element $u_i^{(2)}$ in $\boldsymbol{u}^{(2)}$. Consequently, the set $\boldsymbol{u}^{(2)}$ can be interpreted as a function, denoted as $f_{\boldsymbol{u}^{(2)}} : \mathscr{P} \rightarrow \boldsymbol{u}^{(2)}$. Then, the calculation of $\bar{\boldsymbol{u}}$ and $\mathscr{P}_{\bar{\boldsymbol{u}}}$ can be achieved through the following process

$$\bar{\boldsymbol{u}} = \text{sort}\left(\boldsymbol{u}^{(2)}\right) \tag{12}$$

$$\mathscr{P}_{\bar{\boldsymbol{u}}} = f_{\boldsymbol{u}^{(2)}}^{-1}\left(\bar{\boldsymbol{u}}\right) \tag{13}$$

where $\text{sort}(\cdot)$ represents a sorting operation that arranges elements in ascending order, and $f_{\boldsymbol{u}^{(2)}}^{-1}(\cdot)$ is the inverse function of $f_{\boldsymbol{u}^{(2)}}(\cdot)$.

Similarly, $\mathscr{P}_{\bar{\boldsymbol{u}}}$ can also be regarded as a function, denoted as $f_{\mathscr{P}} : \mathscr{L} \rightarrow \mathscr{P}_{\bar{\boldsymbol{u}}}$, where $\mathscr{L}$ represents the position vector, which consists of the positions of each element of $\mathscr{P}_{\bar{\boldsymbol{u}}}$ in $\mathscr{P}_{\bar{\boldsymbol{u}}}$. Subsequently, the second-round

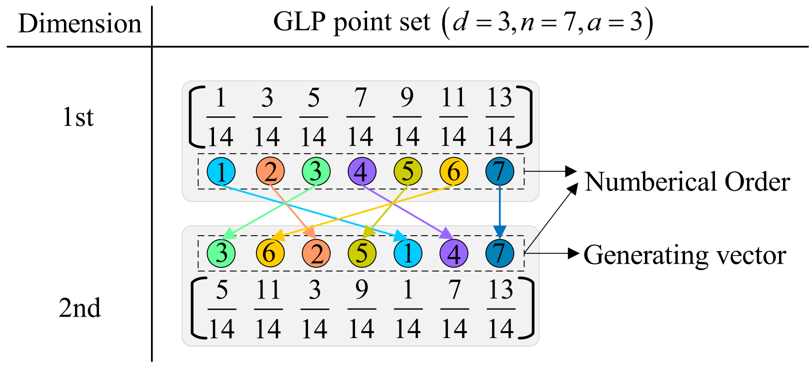

Fig. 3. Principle of operation of DD-GLP method to obtain a point set.

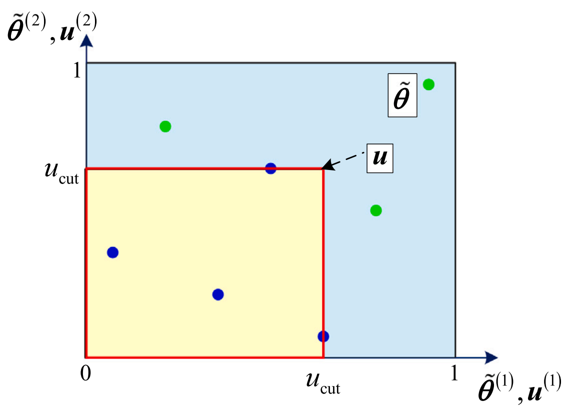

Fig. 4. Schematic diagram of the cutting point set.

sorting operation is executed to arrange the elements in $\mathscr{P}_{\tilde{\mathbf{u}}}$, resulting in the sorted vector $\bar{\mathscr{P}}$. Additionally, the corresponding position vector, denoted as $\mathbf{v}$, of $\bar{\mathscr{P}}$ in $\mathscr{P}_{\tilde{\mathbf{u}}}$ is calculated. This process can be expressed as follows

$$\bar{\mathscr{P}} = \text{sort}\left(\mathscr{P}_{\tilde{\mathbf{u}}}\right) \tag{14}$$

$$\begin{cases} \mathbf{v} = \left(v_1, v_2, \ldots, v_{\bar{q}}, \ldots, v_{n_t}\right) = f_{\mathscr{P}}^{-1}\left(\bar{\mathscr{P}}\right) \\ 0 < v_{\bar{q}} \leq n_t \end{cases}, \quad \bar{q} = 1, 2, \ldots, n_t \tag{15}$$

where $f_{\mathscr{P}}^{-1}(\cdot)$ is the inverse function of $f_{\mathscr{P}}(\cdot)$.

Through Eqs. (12), (13), (14), and (15), the numerical order of $\boldsymbol{u}^{(2)}$, denoted as $\mathbf{v}$, is determined. As explained earlier, the term $\mathbf{v}$ in Eq. (15) possesses the property of a generating vector $\mathbf{h}$ Eq. (1). Consequently, $\mathbf{v}$ can be specifically treated as a generating vector for constructing a uniform point set with n_t points. The schematic representation of this two-round sorting strategy is illustrated in Fig. 6. For the specific example mentioned above, the new generating vector $\mathbf{v}$ can be calculated using the proposed method as $\mathbf{v} = [3, 2, 4, 1]$.

The suggested two-round sorting strategy for constructing the generating vector eliminates the need for primitive root optimization and congruence calculations in high-dimensional point sets with a large number of points. Consequently, it circumvents the NP-hard problem and the iterative process, making the proposed method computationally efficient and highly robust.

3.3. Generation of the representative point set

Once the generating vector $\mathbf{v}$ is determined, the points of the remaining dimensions $\tilde{\boldsymbol{u}}^{(i)}$ in the proposed uniform point set $\mathcal{P}_{\tilde{\mathbf{u}}} = \left\{\tilde{\boldsymbol{u}}_{\bar{q}} = \left(\tilde{u}_{\bar{q}}^{(1)}, \tilde{u}_{\bar{q}}^{(2)}, \ldots, \tilde{u}_{\bar{q}}^{(d)}\right),\ \bar{q} = 1, 2, \ldots, n_t\right\}$ can be recursively derived by the dimension-by-dimension mapping, starting from the points of the first dimension $\tilde{\boldsymbol{u}}^{(1)}$. In this context, the calculation of $\tilde{\boldsymbol{u}}^{(1)}$ should be carried out first using either Eq. (2) or Eq. (3) as follows

$$\begin{aligned} \tilde{\boldsymbol{u}}^{(1)} &= \left(\tilde{u}_1^{(1)}, \tilde{u}_2^{(1)}, \ldots, \tilde{u}_{\bar{q}}^{(1)}, \ldots, \tilde{u}_{n_t}^{(1)}\right)^T \\ &= \left(\frac{1}{2n_t}, \frac{3}{2n_t}, \ldots, \frac{2\bar{q}-1}{2n_t}, \ldots, \frac{2n_t-1}{2n_t}\right)^T, \bar{q} = 1, 2, \ldots, n_t \end{aligned} \tag{16}$$

Subsequently, in accordance with the DD-GLP, the $\bar{q}$th point of the ith dimension in the proposed uniform point set $\mathcal{P}_{\tilde{\mathbf{u}}}$, denoted as $\tilde{u}_{\bar{q}}^{(i)}$, can be obtained from the $v_{\bar{q}}$th point of the $(i-1)$th dimension of $\mathcal{P}_{\tilde{\mathbf{u}}}$. This relationship can be expressed as

$$\tilde{u}_{\bar{q}}^{(i)} = \tilde{u}_{v_{\bar{q}}}^{(i-1)},\ \bar{q} = 1, 2, 3, \ldots, n_t;\ i = 1, 2, 3, \ldots, d \tag{17}$$

Let us continue with the above example to illustrate this. The first dimension of the proposed uniform point set $\tilde{\boldsymbol{u}}^{(1)}$ can be computed using Eq. (16), resulting in $\tilde{\boldsymbol{u}}^{(1)} = (1/8, 3/8, 5/8, 7/8)^T$. Subsequently, the entire point set $\tilde{\boldsymbol{u}}$ can be directly obtained using Eq. (17) as follows:

$$\tilde{\boldsymbol{u}} = \begin{pmatrix} 1/8 & 5/8 & 7/8 \\ 3/8 & 3/8 & 3/8 \\ 5/8 & 7/8 & 1/8 \\ 7/8 & 1/8 & 5/8 \end{pmatrix} \tag{18}$$

The schematic diagram illustrating the process of generating the proposed uniform point set is presented in Fig. 7.

It can be seen that the generation of a target uniform d-dimensional point set $\mathcal{P}_{\tilde{\mathbf{u}}}$ with n_t points through the proposed method involves two main steps: (1) obtaining the generating vector $\mathbf{v}$ using the cutting method and the two-round sorting strategy; and (2) generating the points in the first dimension with Eq. (16), followed by the recursive generation of points in the remaining dimensions using Eq. (17). It is noteworthy that the proposed method distinguishes itself by not requiring the generation of an initial point set in the high-dimensional space through the GLP method or DD-GLP method. Instead, it only relies on a two-dimensional initial point $\mathcal{P}_{\tilde{\boldsymbol{\theta}}}$, thereby avoiding the limitations associated with the GLP method or DD-GLP method.

Upon obtaining the proposed uniform point set $\mathcal{P}_{\tilde{\mathbf{u}}}$, the representative point set $\mathcal{P}_{\boldsymbol{x}} = \left\{\boldsymbol{x}_{\bar{q}} = \left(x_{\bar{q}}^{(1)}, x_{\bar{q}}^{(2)}, \ldots, x_{\bar{q}}^{(d)}\right),\ \bar{q} = 1, 2, \ldots, n_t\right\}$ in the original random variate space can be obtained through isoprobabilistic transformation

$$x_{\bar{q}}^{(i)} = \mathcal{F}^{-1}\left(\mathcal{Y}_{\tilde{\mathbf{u}}}\left(\tilde{u}_{\bar{q}}^{(i)}\right)\right) = \mathcal{F}^{-1}\left(\tilde{u}_{\bar{q}}^{(i)}\right), i = 1, 2, \ldots, d; \bar{q} = 1, 2, \ldots, n_t \tag{19}$$

where $\mathcal{F}^{-1}(\cdot)$ represents the inverse Cumulative Distribution Function (CDF) of the d independent random variables $\mathbf{X} = \left[X_1, X_2, \ldots, X_d\right] \in \mathcal{X} \subseteq \mathbb{R}^d$, and $\mathcal{Y}_{\tilde{\mathbf{u}}}(\cdot)$ denotes the CDF of the uniform distribution with parameter $[0, 1]$. In cases involving correlated random variables, the representative point set $\mathcal{P}_{\boldsymbol{x}}$ can be obtained through the Nataf transformation [63].

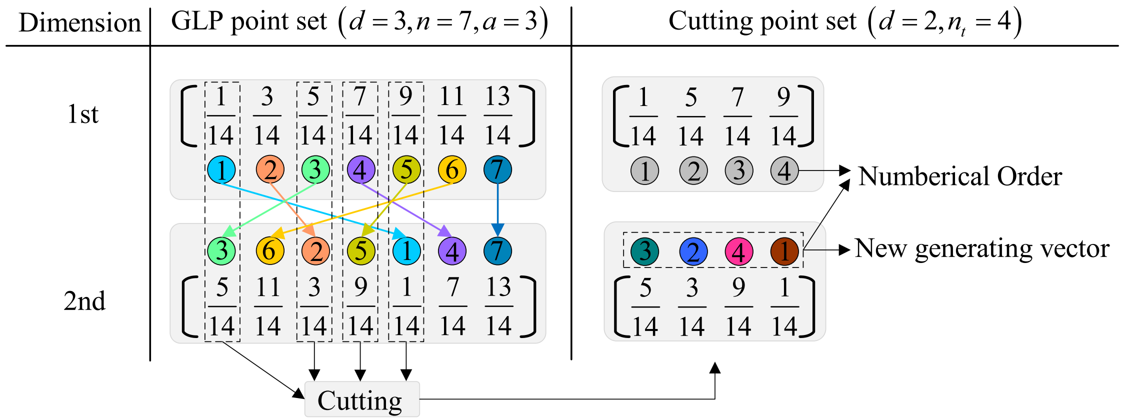

Fig. 5. Schematic diagram of the new generating vector.

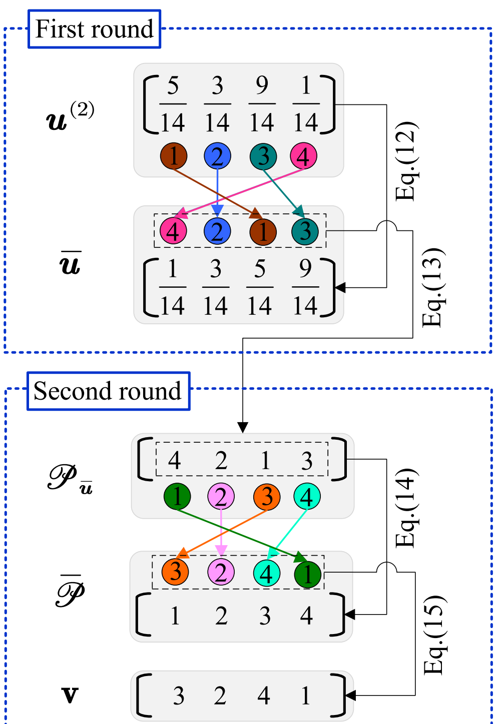

Fig. 6. Schematic diagram of the two-round sorting strategy.

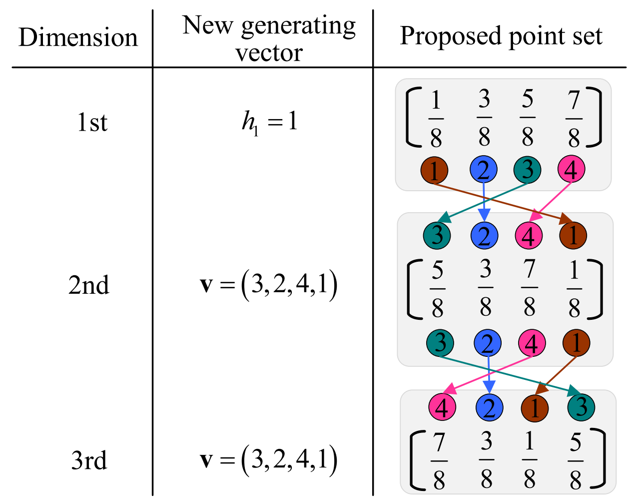

Fig. 7. Schematic diagram of the proposed point set generation process.

Then, the representative point set $\mathcal{P}_x$ can be used as the set of input samples for accurate statistical moment estimation and high-dimensional reliability assessment, as described in the subsequent sections.

4. High-dimensional reliability analysis of structures

4.1. Problem statement

Structural reliability refers to the capacity of the structure to fulfill expected safety, applicability, and durability requirements under specified conditions, considering inherent uncertainties. Let $\mathbf{X} = [X_1, X_2, \ldots, X_d] \in \mathcal{X} \subseteq \mathbb{R}^d$ represent a vector of d random variables, serving as models for uncertain inputs in a LSF. The LSF, denoted as $Z = G(\mathbf{X}) : \mathbb{R}^d \to \mathbb{R}$, takes on a value $z = G(\mathbf{X}) \le 0$ to indicate a failure state, and otherwise, a safe state. Without loss of generality, the LSF $Z = G(\mathbf{X})$ can be expressed by the following equation

$$Z = G(\mathbf{X}) = R(\mathbf{X}) - S(\mathbf{X}) \tag{20}$$

where $R(\cdot)$ and $S(\cdot)$ represent the capacity and demand, respectively.

By substituting the points of the representative point set $\mathcal{P}_x$ into Eq. (20), the samples of the LSF can be obtained. Subsequently, once the PDF of the LSF, denoted as $f_Z(z)$, is derived, the corresponding failure probability of the LSF can be calculated using

$$P_f = \mathrm{Prob}(Z \le 0) = \int_{-\infty}^{0} f_Z(z)\,\mathrm{d}z \tag{21}$$

where $\mathrm{Prob}(\cdot)$ denotes the probability and the generalized reliability index β is determined by

$$\beta = -\Phi^{-1}\left(P_f\right) \tag{22}$$

where $\Phi^{-1}(\cdot)$ represents the inverse CDF of the standard Gaussian distribution.

The focus, then, shifts to deriving the PDF $f_Z(z)$ of the LSF. Analytically deriving the PDF $f_Z(z)$ of LSF is generally challenging for high-dimensional problems. In the next section, the FEM-MEM [53] and Box–Cox transformation [64,65] are introduced as numerical approaches to reconstruct the PDF $f_Z(z)$ of the LSF, based on the samples of LSF.

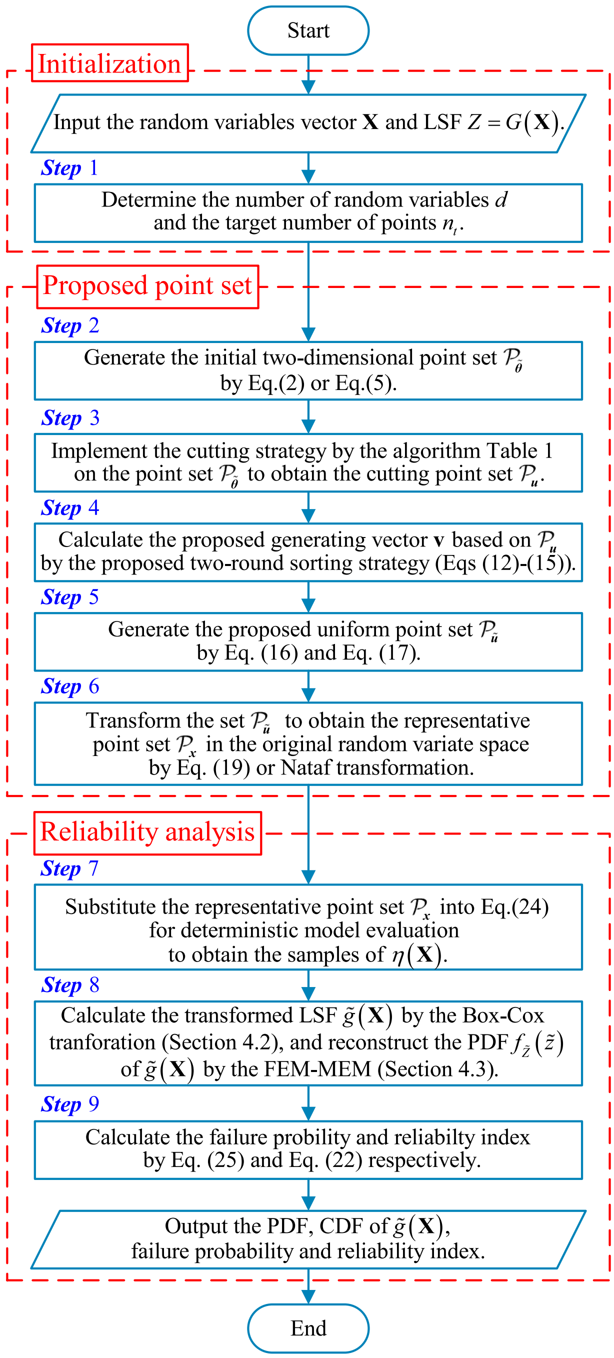

Fig. 8. Flowchart of the proposed method.

4.2. Box–Cox transformation

It is widely acknowledged that the FM-MEM stands out as one of the most accurate estimators for an unknown PDF [66]. The enhanced version, FEM-MEM [53], has gained popularity in the reliability analysis community due to its improved robustness and efficiency [24,54]. Therefore, this paper introduces FEM-MEM in Section 4.3 to numerically reconstruct the PDF $f_Z(z)$ of the LSF. However, it is worth noting that while FEM-MEM is a powerful tool for reconstructing unknown probability distributions, it may exhibit inaccuracies when dealing with PDFs featuring long tails [14]. To address this, the Box–Cox transformation [64,65] is initially applied. This transformation serves to convert the probability distribution of the LSF into either a normal or weakly non-normal distribution, ensuring the accuracy and robustness of the subsequent FEM-MEM reconstruction.

By employing the Box–Cox transformation, Eq. (20) can be equivalently expressed as

$$\tilde{g}(\mathbf{X}) = \begin{cases} \frac{\eta(\mathbf{X})^{\kappa}-1}{\kappa}, & \kappa \neq 0 \\ \ln[\eta(\mathbf{X})], & \kappa = 0 \end{cases} \tag{23}$$

where

$$\eta(\mathbf{X}) = \frac{R(\mathbf{X})}{S(\mathbf{X})} \tag{24}$$

and κ represents the transformation parameter.

To balance the accuracy and efficiency, the parameter κ is determined when $\left|\alpha_{3,\tilde{g}}\right| \leq 0.1$ is satisfied, where $\alpha_{3,\tilde{g}}$ denotes the skewness of the transformed LSF $\tilde{g}(\mathbf{X})$. Specifically, this determination can be carried out through enumeration, in which the range of κ limits to $[-1, 1]$ [65], with a step size of 2×10^{-5}. Substituting each $\kappa \in \left[-1 : 2 \times 10^{-5} : 1\right]$ into Eq. (23), the final value of κ is selected once the condition $\left|\alpha_{3,\tilde{g}}\right| \leq 0.1$ is satisfied.

Although a Box–Cox transformation has been applied to the LSF $G(\mathbf{X})$, the limit states of $G(\mathbf{X})$ and $\tilde{g}(\mathbf{X})$ remain consistent. Up to this point, the failure probability of $G(\mathbf{X})$ can be calculated by the transformed LSF $\tilde{g}(\mathbf{X})$ as follows

$$P_f = \int_{-\infty}^{0} f_{\tilde{Z}}(\tilde{z})\, d\tilde{z} \tag{25}$$

where $\tilde{Z} = \tilde{g}(\mathbf{X})$ and its PDF is $f_{\tilde{Z}}(\tilde{z})$.

4.3. Probability distribution reconstruction by FEM-MEM

Indeed, the transformed LSF $\tilde{g}(\mathbf{X})$ can be regarded as a random variable, denoted as $\tilde{Z}$. Since the distribution domains of $\tilde{Z}$ may vary across different problems, scale transformation and translation transformation [53] are initially performed to convert $\tilde{Z}$ into a positively bounded variable Y. The details of these two transformation steps can be found in the Ref. [53].

Generally, the FEMs of Y is defined as [53]

$$\mathbb{E}\left[\exp\left(-\alpha_k y\right)\right] = \int_{\Omega_Y} \exp\left(-\alpha_k y\right) p_Y(y)\, \mathrm{d}y \tag{26}$$

where α_k represents the fractional order, Ω_Y denotes the distribution domain of Y and $f_Y(y)$ represents the PDF of Y. Utilizing the representative point set $\mathcal{P}_{\boldsymbol{x}}$ transformed by the proposed point set $\mathcal{P}_{\tilde{\boldsymbol{u}}}$, the fractional order moments of Y can be numerically computed by

$$\mathbb{E}\left[\exp\left(-\alpha_k y\right)\right] \approx \sum_{\tilde{q}=1}^{n_t} \frac{\exp\left(-\alpha_k y\left(\boldsymbol{x}_{\tilde{q}}\right)\right)}{n_t} \tag{27}$$

Subsequently, the PDF of Y, $f_Y(y)$, can be obtained by solving an optimization problem with a total of K constraints [67,68], which can be formulated as follows

$$\begin{cases} \text{Find} \ : \ \lambda = \left[\lambda_1, \lambda_2, \ldots, \lambda_K\right]^T \ \text{and} \ \alpha^* \\ \text{Minimize:} \ \mathcal{L}(\alpha^*, \lambda) = \ln\left\{\int_{\Omega_Y} \exp\left[-\sum_{k=1}^{K} \lambda_k \exp\left(-k\alpha^* \cdot y\right)\right] \mathrm{d}y\right\} + \sum_{k=1}^{K} \lambda_k M_Y^{k\alpha^*} \\ s.t. \ -2 \leq \alpha^* \leq 2 \end{cases} \tag{28}$$

where α^* is the optimal fractional order, $\boldsymbol{\alpha} = [\alpha^*, 2\alpha^*, 3\alpha^*, \ldots, K\alpha^*]^T$ is the fractional order vector, $M_Y^{k\alpha^*}, k = 1, 2, \ldots, K$ denotes the sample FEM, $\lambda = [\lambda_1, \lambda_2, \ldots, \lambda_K]^T$ is the vector of Lagrange multipliers, which can be calculated by a linear mathematical operation [69].

Correspondingly, the PDF of Y can be represented as follows

$$f_Y(y) = \exp\left[-\lambda_0 - \sum_{k=1}^{K} \lambda_k \exp\left(-\alpha_k y\right)\right] \tag{29}$$

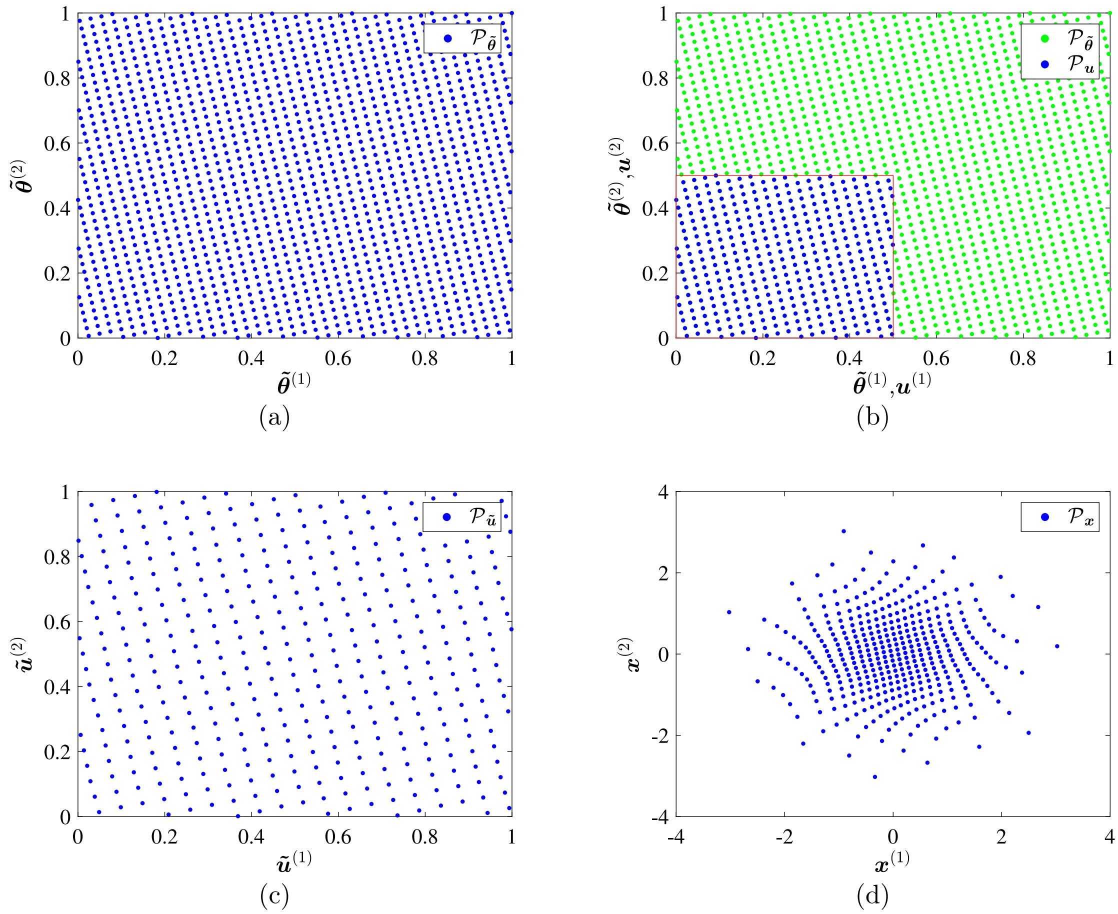

Fig. 9. Points in the first two dimensions (Example 1).

where

$$\lambda_0 = \ln\left\{\int_{\Omega_Y} \exp\left[-\sum_{k=1}^{K} \lambda_k \exp\left(-\alpha_k y\right)\right] \mathrm{d}y\right\} \tag{30}$$

Once the PDF $f_Y(y)$ is obtained, the PDF $f_{\tilde{Z}}(\tilde{z})$ of the transformed LSF $\tilde{g}(\mathbf{X})$ can be determined through linear translation and scale transformation [69].

5. Step-by-step procedure of the proposed method

In summary, a deterministic sampling method for high-dimensional reliability analysis of structures is proposed in the present paper, whose calculation procedure flowchart is depicted in Fig. 8. The corresponding detailed steps are outlined below:

Step 1: Determine the number of random variables d and the target number of points n_t.

Step 2: Generate the initial two-dimensional point set $\mathcal{P}_{\tilde{\theta}} = \left\{\tilde{\boldsymbol{\theta}}_q = \left(\tilde{\theta}_q^{(1)}, \tilde{\theta}_q^{(2)}\right),\ q = 1, 2, \ldots, n\right\}$ with parameters $n = 1597, a = 679$ using Eq. (2) or Eq. (5).

Step 3: Implement the cutting strategy (Table 1) to obtain the two-dimensional cutting point set $\mathcal{P}_{\boldsymbol{u}} = \left\{\boldsymbol{u}_{\bar{q}} = \left(u_{\bar{q}}^{(1)}, u_{\bar{q}}^{(2)}\right),\ \bar{q} = 1, 2, \ldots, n_t\right\}$ with n_t points from the initial two-dimensional point set $\mathcal{P}_{\tilde{\theta}}$.

Step 4: Extract the points in the second dimension of the cutting point set $\mathcal{P}_{\boldsymbol{u}}$ and apply the proposed two-round sorting strategy (Eqs. (12), (13), (14), and (15)) to construct the new generating vector $\mathbf{v}$ for generating the d-dimensional uniform point set $\mathcal{P}_{\tilde{\boldsymbol{u}}} = \left\{\tilde{\boldsymbol{u}}_{\bar{q}} = \left(\tilde{u}_{\bar{q}}^{(1)}, \tilde{u}_{\bar{q}}^{(2)}, \ldots, \tilde{u}_{\bar{q}}^{(d)}\right),\ \bar{q} = 1, 2, \ldots, n_t\right\}$.

Step 5: Utilize the GLP or DD-GLP method to generate the n_t points in the first dimension Eq. (16), and obtain the proposed uniform point set $\mathcal{P}_{\tilde{\boldsymbol{u}}}$ across the entire d-dimensional unit hypercube space using the dimension-by-dimension mapping strategy iteratively Eq. (17).

Step 6: Transform the proposed uniform point set $\mathcal{P}_{\tilde{\boldsymbol{u}}}$ using isoprobabilistic transformation Eq. (19) or Nataf transformation to obtain the representative point set $\mathcal{P}_{\boldsymbol{x}} = \left\{\boldsymbol{x}_{\bar{q}} = \left(x_{\bar{q}}^{(1)}, x_{\bar{q}}^{(2)}, \ldots, x_{\bar{q}}^{(d)}\right),\ \bar{q} = 1, 2, \ldots, n_t\right\}$ in the original random variate space.

Step 7: Substitute the representative point set $\mathcal{P}_{\boldsymbol{x}}$ into Eq. (24) to calculate the samples of the interested physical quantity of structures by repeatedly performing deterministic model evaluations.

Step 8: Apply the Box–Cox transformation to transform the LSF $G(\mathbf{X})$ into $\tilde{g}(\mathbf{X})$ (as described in Section 4.2), and use FEM-MEM (as described in Section 4.3) to calculate the PDF $f_{\tilde{Z}}(\tilde{z})$ of $\tilde{g}(\mathbf{X})$.

Step 9: Compute the failure probability and reliability index by integrating the PDF $f_{\tilde{Z}}(\tilde{z})$ of the transformed LSF $\tilde{g}(\mathbf{X})$. This can be done using Eqs. (22) and (25), respectively.

6. Numerical examples

This section presents three high-dimensional numerical examples, featuring both explicit and implicit LSFs, to illustrate the versatility and effectiveness of the proposed method in high-dimensional reliability analysis. Additionally, correlated random variables are considered in the second example. Alongside, the MCS and other prominent methods in the field are leveraged, including the FORM, SORM, SS, and IS, as available in UQlab [70], to compare and highlight the strengths of the

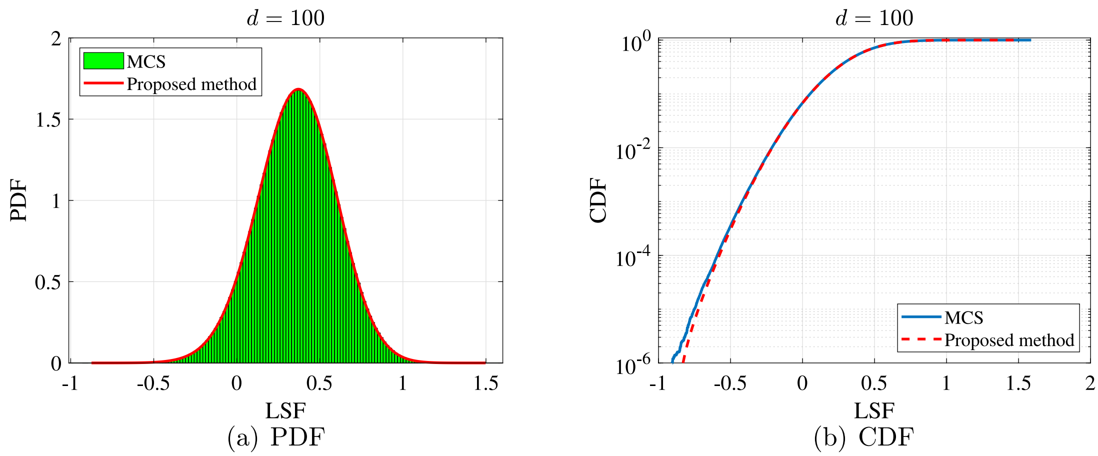

Fig. 10. PDF and CDF of transformed LSF (Example 1, $d = 100$).

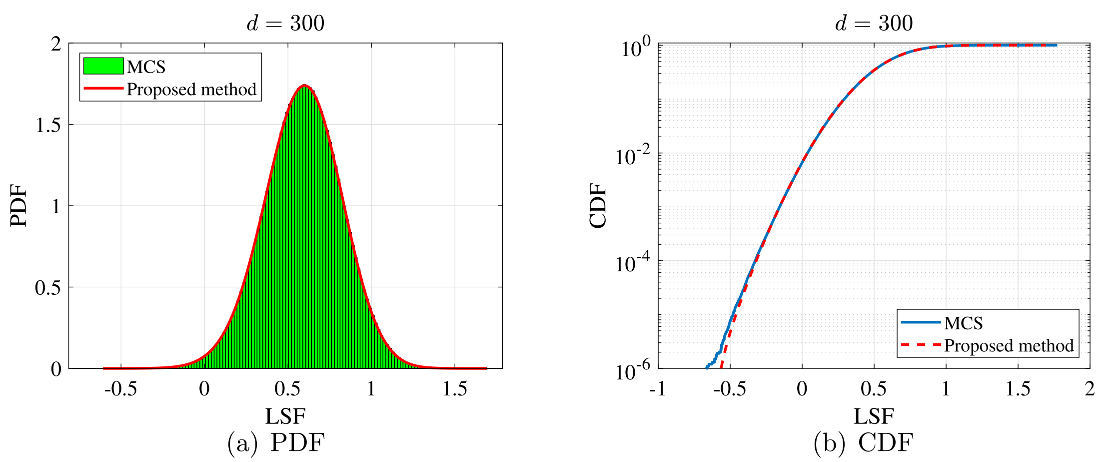

Fig. 11. PDF and CDF of transformed LSF (Example 1, $d = 300$).

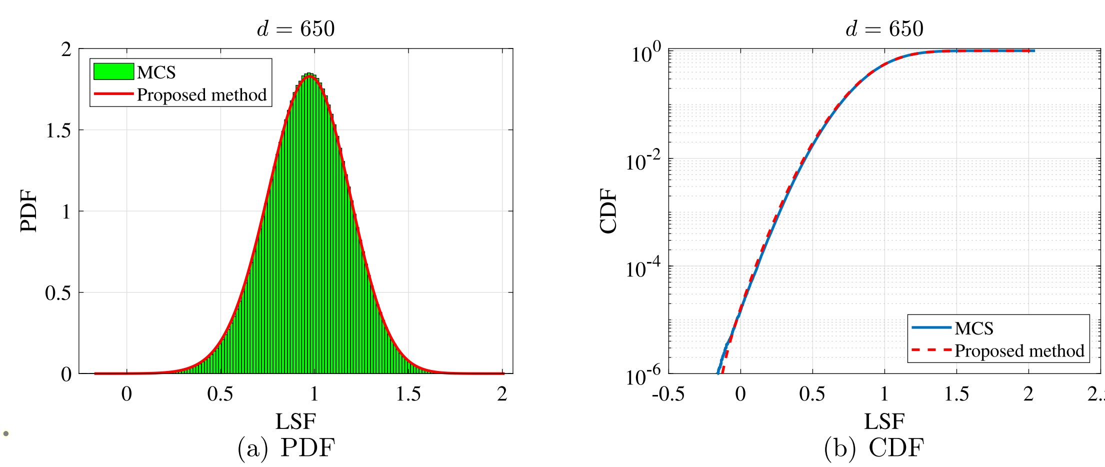

Fig. 12. PDF and CDF of transformed LSF (Example 1, $d = 650$).

Table 2
Comparison of reliability analyses (Example 1).

Dimension	Method	n_t	$\hat{\beta}$	$e_{\hat{\beta}}$ (%)	$\hat{P}_f$	$e_{\hat{P}_f}$ (%)	C.O.V
100	MCS	1×10^7	1.4897	–	6.8149×10^{-2}	–	0.0012
	FORM	204	1.0000	32.873	1.5866×10^{-1}	132.8155	–
	SS	1900	1.5001	0.6939	6.6800×10^{-2}	1.9796	0.1054
	IS	1204	1.5172	1.5436	6.5176×10^{-2}	4.3623	0.0554
	Sobol Point	400	1.4741	1.0482	7.0227×10^{-2}	3.0490	–
	Proposed	400	1.4927	0.1996	6.7759×10^{-2}	0.5725	–
300	MCS	1×10^7	2.4756	–	6.6502×10^{-3}	–	0.0039
	FORM	604	1.0000	59.606	1.5866×10^{-1}	–	–
	SS	2800	2.5284	2.1298	5.7300×10^{-3}	13.8369	0.2088
	IS	1604	2.5290	2.1551	5.7203×10^{-3}	13.9906	0.1320
	Sobol Point	400	2.6023	5.1166	4.6302×10^{-3}	30.3755	–
	Proposed	400	2.4703	0.2163	6.7506×10^{-3}	1.5095	–
650	MCS	1×10^7	4.1731	–	1.5021×10^{-5}	–	0.0816
	FORM	1304	1.0000	76.037	1.5887×10^{-1}	–	–
	SS	4600	4.1409	0.7734	1.7300×10^{-5}	15.1683	0.3784
	IS	2304	–	–	–	–	–
	Sobol Point	400	4.3516	4.2771	6.7564×10^{-6}	55.0215	–
	Proposed	400	4.1514	0.5200	1.6519×10^{-5}	9.9712	–

Note: C.O.V = Coefficient of variation.

Table 3
Star discrepancy comparison of Point Sets (Example 1)..

Dimension	GLP			Propsoed method		
	n	a	Star discrepancy	n_t (n)	a	Star discrepancy
2	233	143	0.0086	233 (1597)	679	0.0059
3	1459	1005	0.0036			0.0183
10	19 069	697	0.0037			0.0515
30	76 673	209	0.0034	400 (1597)	679	0.1064
50	123 121	244	0.0064			0.0899
100	354 017	54	0.0099			0.0774

considered methods. These benchmark methods are run in their default configurations unless specified otherwise.

6.1. Example 1

In the first example, the performance of the proposed method is investigated by a high-dimensional nonlinear LSF with different dimensions, as follows

$$Z = G(\mathbf{X}) = \left(5 + 0.005\sum_{j=1}^{d-1} X_j^2 - X_d\right) - 4 \tag{31}$$

where X_j, $j = 1, 2, \ldots, d$ are independent standard normal random variables.

To clearly illustrate the execution of the proposed method, a step-by-step computational flow corresponding to the procedure in Section 5 and Fig. 8 is provided as follows:

***Step* 1 :** In this example, three distinct cases with dimensions d =100, 300, and 650 are considered. Each case involves a total of n_t = 400 points.

***Step* 2 :** Initially, a two-dimensional point set $\mathcal{P}_{\tilde{\theta}}$ comprising 1597 samples is generated via the DD-GLP method, as illustrated in Fig. 9(a).

***Step* 3 :** Subsequently, a subset of 400 samples, referred to as the cutting point set $\mathcal{P}_{\boldsymbol{u}}$, is extracted from $\mathcal{P}_{\tilde{\theta}}$ using the cutting method. This step is depicted in Fig. 9(b).

***Step* 4 :** Based on $\mathcal{P}_{\boldsymbol{u}}$, a new generating vector $\mathbf{v}$ is calculated using the equations outlined in (12), (13), (14), and (15). The values of $\mathbf{v}$ are tabulated in Table A.6 Appendix.

***Step* 5 :** For the first dimension, the 400 points are computed using the GLP method, as per Eq. (16). The points in subsequent dimensions are recursively determined using the generating vector $\mathbf{v}$, culminating in the formation of the proposed point set $\mathcal{P}_{\tilde{\boldsymbol{u}}}$, which consists of 400 points within the unit hypercube space $[0,1]^d$. Fig. 9(c) showcases the first two-dimensions of $\mathcal{P}_{\tilde{\boldsymbol{u}}}$.

***Step* 6 :** The obtained point set $\mathcal{P}_{\tilde{\boldsymbol{u}}}$ is, then, transformed into the representative point set $\mathcal{P}_{\boldsymbol{x}}$ within the original random variate space. This transformation, an essential step in the process, is visualized in Fig. 9(d).

***Step* 7 :** The representative point set $\mathcal{P}_{\boldsymbol{x}}$ is then input into the LSF for deterministic model evaluations, yielding LSF response samples.

***Step* 8 :** Afterward, the Box–Cox transform is applied to obtain the transformed LSF. Subsequently, the PDF and CDF of the transformed LSF are reconstructed using the FEM-MEM, as shown in Figs. 10, 11, and 12.

***Step* 9 :** Finally, the failure probability and reliability index can be calculated based on the reconstructed PDF of the LSF, as presented in Table 2.

The recovered PDFs and CDFs in logarithmic scale of the transformed LSFs for these three cases are depicted in Figs. 10, 11, and 12, juxtaposed with results from 10^7 MCS runs for comparative purposes. These figures attest to the strong accordance between the results from the proposed method and the MCS, confirming the ability of the proposed method to accurately approximate LSFs' probability distributions.

The estimated reliability indices $\hat{\beta}$ and failure probabilities $\hat{P}_f$, as obtained by the proposed method and other known methods, are listed in Table 2. Notably, the FORM, despite requiring fewer deterministic model calculations than the proposed method, fails to yield satisfactory results in this numerical example. In contrast, the IS and SS methods, although nearly matching the reference results, demand thousands of deterministic model evaluations and exhibit some variability. The proposed method stands out, requiring merely 400 evaluations for

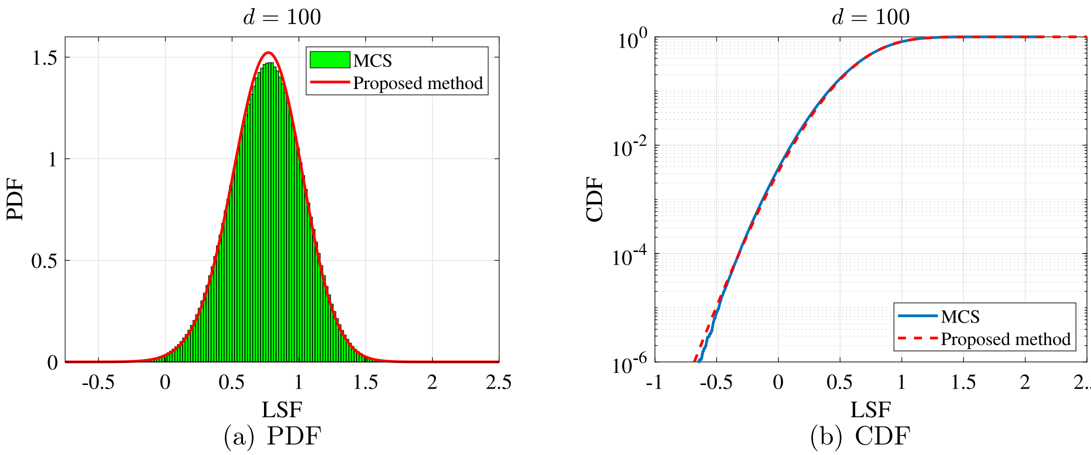

Fig. 13. PDF and CDF of transformed LSF (Example 2, $d = 100$).

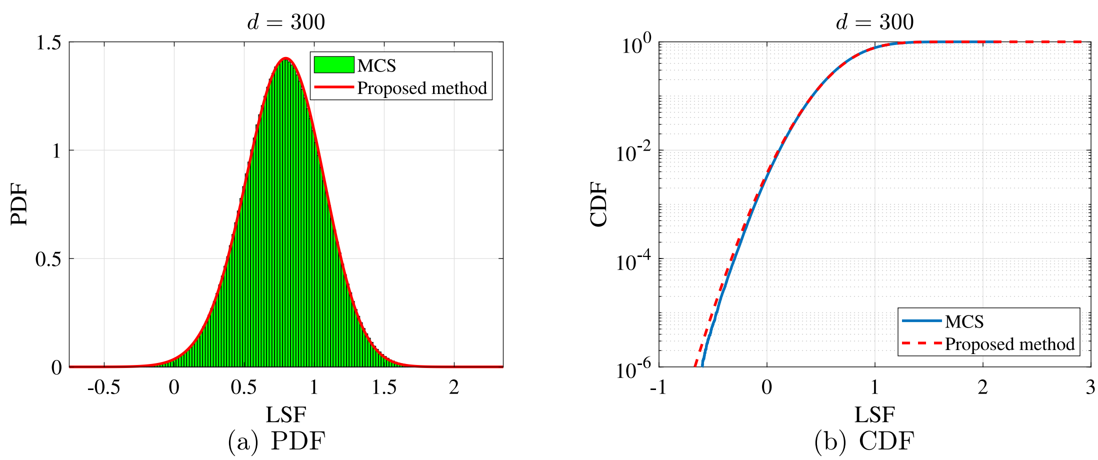

Fig. 14. PDF and CDF of transformed LSF (Example 2, $d = 300$).

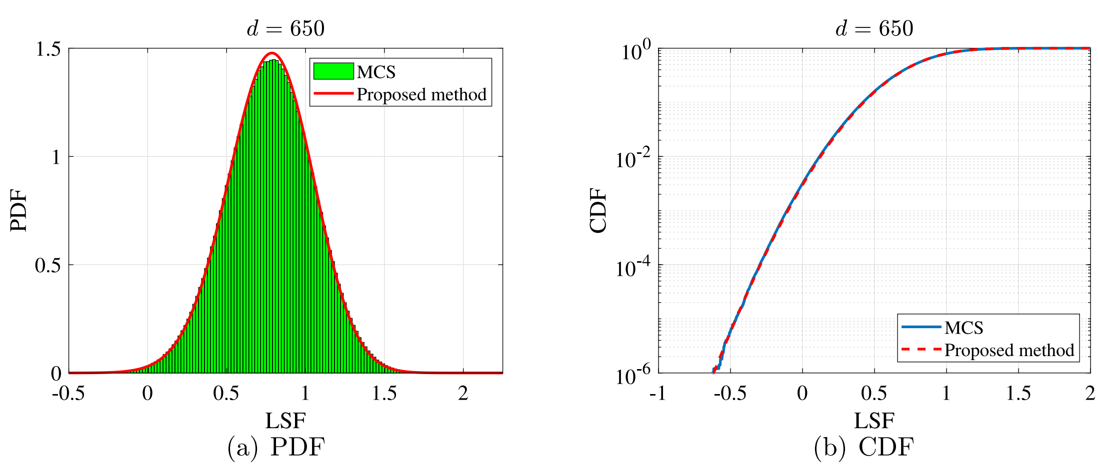

Fig. 15. PDF and CDF of transformed LSF (Example 2, $d = 650$).

higher accuracy and consistency. If efficiency is measured by the number of LSF calls, the proposed method is markedly more efficient, requiring only 400 calculations compared to the thousands or more needed by the other methods listed in Table 2. Furthermore, we benchmarked against the Sobol sequence method with 400 samples, and the proposed method demonstrated superior computational efficiency and comparable accuracy in high-dimensional reliability analysis. The failure probabilities produced by the proposed method and MCS closely match in each scenario, verifying the proposed method's effectiveness. Remarkably, the consistent use of 400 samples across all three cases implies that the proposed method's performance is largely unaffected by dimensionality. This is further highlighted in the evaluation of small failure probabilities (around 10^{-5}) in a 650-dimensional problem, achieved with just 400 model evaluations, showcasing remarkable efficiency. Additionally, the proposed method may address the "curse of dimensionality”, as it inherently benefits from the NTM, maintaining a constant number of model evaluations regardless of dimension.

Additionally, to investigate the uniformity of point sets generated by the proposed method (with $n_t = 400$, $n = 1597$, $a = 679$), the star discrepancies of these point sets are compared with that of the GLP point sets across different dimensions ($d = 2, 3, 10, 30, 50, 100$). The corresponding results are presented in Table 3. For these GLP point sets, the number of points n and the primitive roots a utilized for different dimensions are based on Ref. [60]. The results in Table 3 show that while the star discrepancies of the point sets generated by the proposed method are slightly higher than that of the GLP point sets in dimensions greater than two, they remain sufficiently small, thus providing a basis for ensuring the accuracy of reliability analysis. Moreover, the sample sizes of the proposed point sets are significantly reduced compared to the GLP point sets, which is essential for maintaining efficiency in high-dimensional reliability analysis. On the other hand, since the uniform point sets generated by the proposed method and the GLP point sets are derived from different generating vectors, establishing a quantitative relationship between their discrepancies across various dimensions poses challenges. Nevertheless, this remains an important issue for future research.

6.2. Example 2

In the second example, a high-dimensional, non-linear limit state function (LSF) with significant skewness and involving correlated random variables is considered, expressed as

$$Z = G(\mathbf{X}) = \frac{2}{d-1}\sum_{i=1}^{d-1} X_i^2 - X_d \tag{32}$$

where X_i, $i = 1, 2, \ldots, d$ are dependent lognormal random variables with the mean 1 and standard derivation 0.3. The correlation coefficient between each pair of variables is 0.1.

Similarly, this example considers three cases with dimensions (d) of 100, 300, and 650. The proposed method is then applied to the LSF presented in Eq. (32). Given the involvement of correlated random variables in this example, the Nataf transformation is implemented to convert the proposed uniform point set into the representative point set in the original random variate space. Subsequently, utilizing only 400 samples, the proposed method accurately captures the PDFs and CDFs of the transformed LSFs with high-dimensional, correlated random inputs, as evidenced in Figs. 13, 14, and 15. These results demonstrate the efficiency and reliability of the proposed method in handling high-dimensional problems with complex and skewed LSFs involving correlated random variables.

To further validate its advantages in reliability analysis, the proposed method is compared with several existing methods that utilize the Nataf transformation. The reliability indices $\hat{\beta}$ and failure probabilities $\hat{P}_f$ obtained by different methods are presented in Table 4. Notably, the method consistently provides accurate reliability assessments across different dimensions. This demonstrates its ability to balance accuracy and efficiency in high-dimensional reliability analysis, even when considering correlated random variables. These findings underscore the effectiveness of the method, making it a promising tool for practical engineering applications that involve high-dimensional and complex reliability challenges.

6.3. Example 3

To more comprehensively assess the applicability of the proposed method to implicit problems, a thin, solid square plate structure, characterized by dimensions $L_a = L_b = 1$ and thickness $t = 1$, is considered. This structure is analyzed using stochastic finite element analysis as detailed in [11] and illustrated in Fig. 16.

The finite element model built by OpenSEES consists of 16 four-node quadrilateral finite elements representing the plate. In this model,

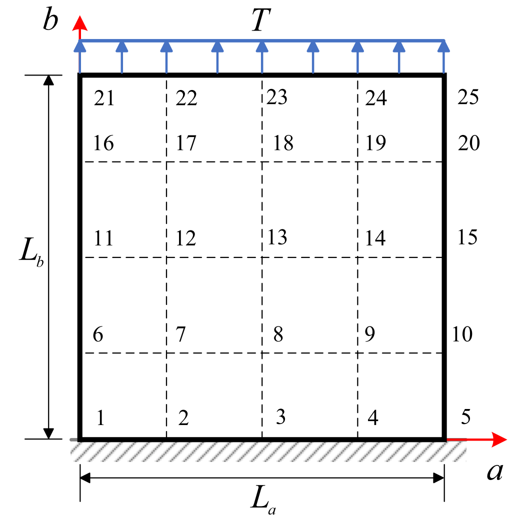

Fig. 16. Schematic view of the thin solid square plate.

one end of the plate is fixed, while the opposite end is subjected to a homogeneous in-plate tension $T = 1$. The Poisson’s ratio of the plate is assumed to be zero, and the Young modulus $\boldsymbol{E}(a, b)$ is described by the two-dimensional Gaussian random field with a mean value μ_E and standard deviation σ_E. The expression for $\boldsymbol{E}(a, b)$ is given as

$$\boldsymbol{E}(a, b) = \mu_E\left[1 + \boldsymbol{\gamma}(a, b)\right] \tag{33}$$

where $\boldsymbol{\gamma}(a, b)$ is a zero-mean stochastic Gaussian random filed with auto-covariance function

$$\rho(a, b) = \sigma_E^2 \exp\left(-\frac{|a_1 - b_1|}{s_1} - \frac{|a_2 - b_2|}{s_2}\right) \tag{34}$$

where s_1 and s_2 are the correlation lengths. The parameters involved in this example are specified as $\mu_E = 1$, $\sigma_E = 0.1$, $s_1 = s_2 = 0.5$. Further, $\boldsymbol{\gamma}(a, b)$ is approximated by the series representation of d independent standard normal variables $\mathbf{X} = \left[X_1, X_2, \ldots, X_d\right]$ using the Karhunen-Love (K-L) expansion:

$$\boldsymbol{\gamma}(a, b) \approx \sum_{i=1}^{d} \sqrt{\varphi_i} X_i \psi_i(a, b) \tag{35}$$

where φ_i and $\psi_i(a, b)$s, $i = 1, 2, \ldots, d$ are the eigenvalues and eigenfunctions of the auto-covariance function $\rho(a, b)$.

In this example, the plate structure is considered to fail when the vertical displacement of node 23, denoted as D_{23}, is larger than the prescribed threshold $\bar{D} = 1.25$. The LSF can be defined as

$$Z = G(\mathbf{X}) = \bar{D} - D_{23}(\mathbf{X}) \tag{36}$$

This example also focuses on three cases to test the applicability of the proposed method for implicit problems with high-dimensional inputs, setting dimensions d at 100, 300, and 650. In each scenario, the proposed method determines a point set of 400 points for reliability analysis. Figs. 17, 18, and 19 illustrate the recovered PDFs and CDFs of the transformed LSFs, compared with MCS results (10^6 runs). These comparisons show notable matching of the PDFs and CDFs obtained by the proposed method and MCS, confirming the method’s capacity to accurately represent the distribution’s main body and tail in implicit problems. Table 5 summarizes the calculated reliability indices and failure probabilities, alongside the results obtained by MCS, FORM, IS, SS, and the Sobol point method. The proposed method stands out for its non-intrusive nature, eliminating the need for gradient information or iterations. Furthermore, it surpasses the accuracy of the Sobol point method with 400 samples, showcasing its effectiveness and precision in high-dimensional reliability problems involving implicit LSFs.

Table 4
Comparison of reliability analyses (Example 2).

Dimension	Method	n_t	$\hat{\beta}$	$e_{\hat{\beta}}$ (%)	$\hat{P}_f$	$e_{\hat{P}_f}$ (%)	C.O.V
100	MCS	1×10^7	2.6760	–	3.7252×10^{-3}	–	0.0052
	FORM	510	2.1754	18.7074	1.4800×10^{-2}	297.2959	–
	SS	2800	2.7349	2.2006	3.1200×10^{-3}	16.2470	0.2097
	IS	1510	2.7279	1.7810	3.2281×10^{-3}	13.6458	0.0704
	Sobol Point	400	2.5159	5.9816	5.9357×10^{-3}	59.3386	–
	Proposed	400	2.7195	1.6268	3.2686×10^{-3}	12.2576	–
300	MCS	1×10^7	2.7159	–	3.3048×10^{-3}	–	0.0055
	FORM	1510	2.2013	18.9493	1.3859×10^{-2}	319.3584	–
	SS	2800	2.6429	2.6878	4.1100×10^{-3}	34.3628	0.2131
	IS	2510	2.7746	2.1618	2.7634×10^{-3}	16.3827	0.0674
	Sobol Point	400	3.0884	13.7170	1.0067×10^{-3}	69.5577	–
	Proposed	400	2.6762	1.4602	3.7227×10^{-3}	12.6439	–
650	MCS	5×10^6	2.7293	–	3.1738×10^{-3}	–	0.0079
	FORM	3260	2.2083	19.0877	1.3611×10^{-2}	328.8637	–
	SS	2800	2.8408	4.0869	2.2500×10^{-3}	29.1075	0.2277
	IS	2304	2.7697	1.4819	2.8053×10^{-3}	11.6100	0.0694
	Sobol Point	400	2.8064	2.8246	2.5053×10^{-3}	21.0636	–
	Proposed	400	2.7496	0.7459	2.9832×10^{-3}	6.0048	–

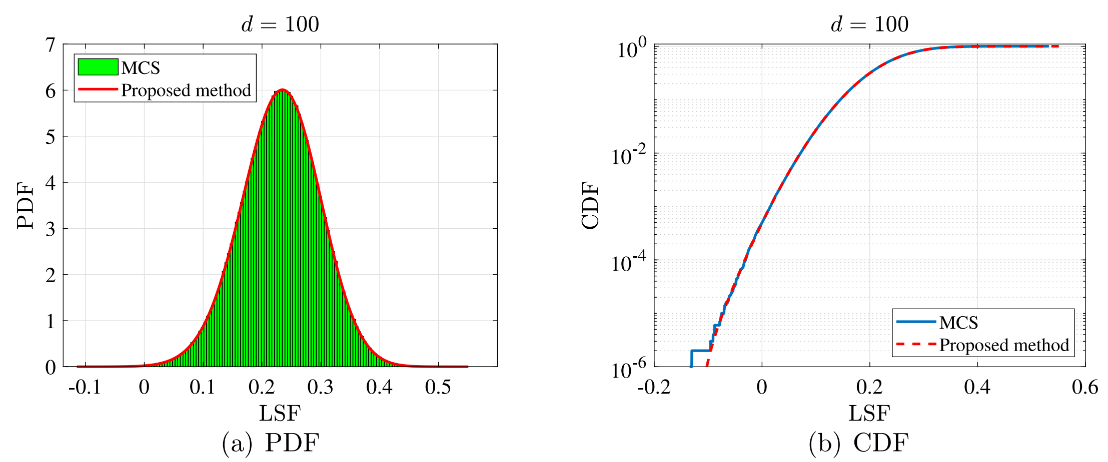

Fig. 17. PDF and CDF of transformed LSF (Example 3, $d = 100$).

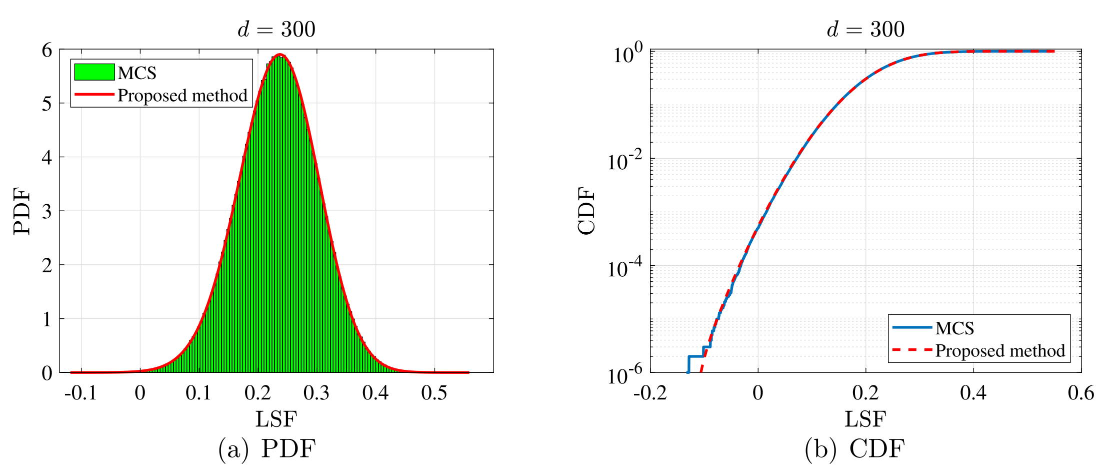

Fig. 18. PDF and CDF of the transformed LSF (Example 3, $d = 300$).

7. Concluding remarks

This work introduces a novel method for high-dimensional uniform point sampling, integrating an innovative generating vector construction technique, the GLP method, and a strategic cutting approach. The methodology involves initially generating a two-dimensional uniform point set via the GLP method. This is followed by employing a cutting strategy to derive a subset of cutting points. Subsequently, a novel two-round sorting strategy is implemented to compute a new generating vector. The point set, generated utilizing this new generating vector, is transformed into the original random variate space, serving as input to the LSF for deterministic model computations. To simplify the reliability analysis, the FEM-MEM combined with a Box–Cox transformation is applied, reconstructing the probability distribution of the transformed

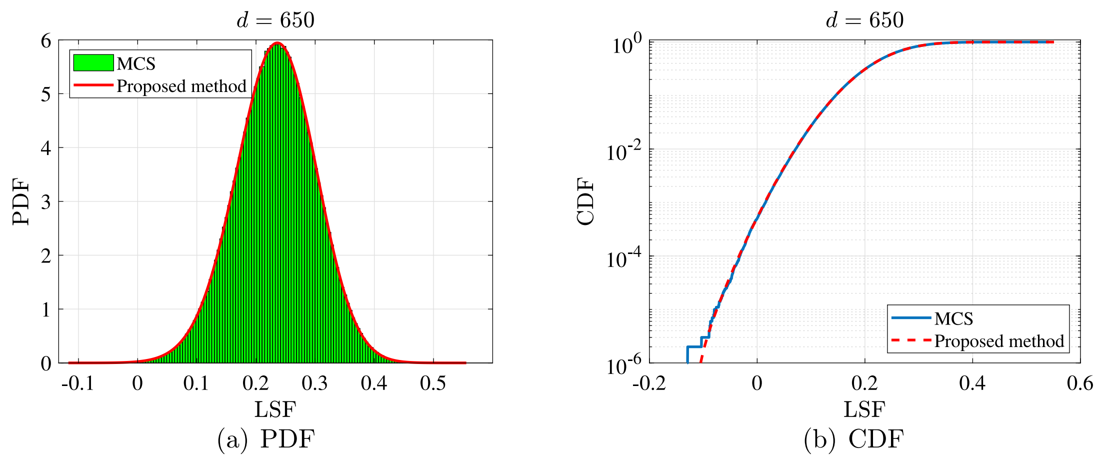

Fig. 19. PDF and CDF of transformed LSF (Example 3, $d = 650$).

Table 5
Comparison of reliability analyses (Example 3).

Dimension	Method	n_t	$\hat{\beta}$	$e_{\hat{\beta}}$ (%)	$\hat{P}_f$ ($\times 10^{-4}$)	$e_{\hat{P}_f}$ (%)	C.O.V
100	MCS	1×10^6	3.2920	–	4.9746	–	0.0448
	FORM	616	3.3568	1.9698	3.9424	20.7483	–
	SS	3700	3.2991	0.2164	4.8500	2.5039	0.2650
	IS	1616	3.2711	0.6345	5.3570	7.6876	0.0583
	Sobol Point	400	3.3221	0.9149	4.4675	10.1938	–
	Proposed	400	3.2955	0.1074	4.9124	1.2493	–
300	MCS	1×10^6	3.2901	–	5.0081	–	0.0447
	FORM	616	3.3544	1.9541	3.9774	20.5803	–
	SS	3700	3.2408	1.4980	5.9600	19.0084	0.3024
	IS	2515	3.3111	0.6396	4.6462	7.2255	0.0631
	Sobol Point	400	3.3149	0.7551	4.5835	8.4772	–
	Proposed	400	3.2697	0.6203	5.3828	7.5019	–
650	MCS	1×10^6	3.2899	–	5.0293	–	0.0466
	FORM	3266	3.3536	1.9671	3.9877	20.6908	–
	SS	3700	3.2968	0.2402	4.8900	2.7700	0.2783
	IS	4266	3.3070	0.5518	4.7145	6.2588	0.0635
	Sobol Point	400	3.3128	0.7272	4.6184	8.1707	–
	Proposed	400	3.2777	0.3412	5.2336	4.0613	–

LSF. The efficacy of this proposed method is substantiated through three numerical examples, yielding the following conclusions:

(1) The proposed method avoids the need for high-dimensional congruence calculations, eliminating the NP-hard problem associated with high-dimensional sampling problems.
(2) The proposed method demonstrates efficiency in generating point sets with an arbitrary number of points, as it eliminates the need for primitive root optimization.
(3) The proposed point set exhibits homogeneity and determinism, contributing to high accuracy and no variability in reliability analysis.
(4) The proposed sampling method utilizes the FEM-MEM method in conjunction with Box–Cox transformation to effectively reconstruct the probability distribution of the LSF, ensuring the robustness of the reliability analysis.
(5) The efficiency of the proposed method is demonstrated by the fact that only 400 points are required for high-dimensional reliability analysis.

The proposed method exhibits the potential to become a valuable tool for the reliability analysis of complex engineering structures characterized by high-dimensional inputs and unimodal failure domain. Future research directions may involve extending the method to tackle reliability analysis problems that involve (1) multimodal failure domains and (2) dynamic challenges associated with short-term dynamic loadings. In addition, this paper does not specifically focus on reliability analysis problems involving non-smooth limit state functions; however, an in-depth exploration of the performance of the proposed method in tackling such issues remains an important topic for future research.

CRediT authorship contribution statement

Yang Zhang: Writing – original draft, Validation, Methodology, Data curation. **Jun Xu:** Writing – original draft, Visualization, Methodology, Investigation, Conceptualization. **Enrico Zio:** Writing – review & editing, Methodology.

Replication of results:

Some or all data, models, or codes generated or used during the study are available from the corresponding author by request.

Declaration of competing interest

The authors declare there is no conflicts of interest regarding the publication of this paper.

Acknowledgments

The authors would like to express our sincere gratitude for the financial support provided by the Open Fund of the State Key Laboratory of Disaster Reduction in Civil Engineering (No. SLDRCE21-04), the National Natural Science Foundation of China (No. 52278178), the

Table A.6
The values of new generating vector **v** for $n_t = 400$.

$\bar{q}$	$v_{\bar{q}}$	$\bar{q}$	$v_{\bar{q}}$	$\bar{q}$	$v_{\bar{q}}$	$\bar{q}$	$v_{\bar{q}}$	$\bar{q}$	$v_{\bar{q}}$	$\bar{q}$	$v_{\bar{q}}$	$\bar{q}$	$v_{\bar{q}}$	$\bar{q}$	$v_{\bar{q}}$	$\bar{q}$	$v_{\bar{q}}$	$\bar{q}$	$v_{\bar{q}}$
1	340	41	352	81	362	121	374	161	385	201	396	241	287	281	298	321	90	361	100
2	220	42	232	82	242	122	254	162	265	202	276	242	167	282	178	322	310	362	320
3	101	43	112	83	122	123	134	163	145	203	156	243	48	283	59	323	190	363	200
4	321	44	332	84	3	124	15	164	26	204	37	244	388	284	399	324	71	364	81
5	201	45	212	85	343	125	355	165	366	205	377	245	268	285	279	325	291	365	301
6	82	46	93	86	223	126	235	166	246	206	257	246	148	286	159	326	171	366	181
7	302	47	313	87	104	127	115	167	126	207	137	247	29	287	40	327	52	367	62
8	182	48	193	88	324	128	335	168	7	208	18	248	369	288	380	328	392	368	282
9	63	49	74	89	204	129	215	169	347	209	358	249	249	289	260	329	272	369	162
10	283	50	294	90	85	130	96	170	227	210	238	250	129	290	140	330	152	370	43
11	163	51	174	91	305	131	316	171	108	211	118	251	10	291	21	331	33	371	383
12	44	52	55	92	185	132	196	172	328	212	338	252	350	292	361	332	373	372	263
13	384	53	395	93	66	133	77	173	208	213	218	253	230	293	241	333	253	373	143
14	264	54	275	94	286	134	297	174	89	214	99	254	111	294	121	334	133	374	24
15	144	55	155	95	166	135	177	175	309	215	319	255	331	295	2	335	14	375	364
16	25	56	36	96	47	136	58	176	189	216	199	256	211	296	342	336	354	376	244
17	365	57	376	97	387	137	398	177	70	217	80	257	92	297	222	337	234	377	124
18	245	58	256	98	267	138	278	178	290	218	300	258	312	298	103	338	114	378	5
19	125	59	136	99	147	139	158	179	170	219	180	259	192	299	323	339	334	379	345
20	6	60	17	100	28	140	39	180	51	220	61	260	73	300	203	340	214	380	225
21	346	61	357	101	368	141	379	181	391	221	281	261	293	301	84	341	95	381	106
22	226	62	237	102	248	142	259	182	271	222	161	262	173	302	304	342	315	382	326
23	107	63	117	103	128	143	139	183	151	223	42	263	54	303	184	343	195	383	206
24	327	64	337	104	9	144	20	184	32	224	382	264	394	304	65	344	76	384	87
25	207	65	217	105	349	145	360	185	372	225	262	265	274	305	285	345	296	385	307
26	88	66	98	106	229	146	240	186	252	226	142	266	154	306	165	346	176	386	187
27	308	67	318	107	110	147	120	187	132	227	23	267	35	307	46	347	57	387	68
28	188	68	198	108	330	148	1	188	13	228	363	268	375	308	386	348	397	388	288
29	69	69	79	109	210	149	341	189	353	229	243	269	255	309	266	349	277	389	168
30	289	70	299	110	91	150	221	190	233	230	123	270	135	310	146	350	157	390	49
31	169	71	179	111	311	151	102	191	113	231	4	271	16	311	27	351	38	391	389
32	50	72	60	112	191	152	322	192	333	232	344	272	356	312	367	352	378	392	269
33	390	73	400	113	72	153	202	193	213	233	224	273	236	313	247	353	258	393	149
34	270	74	280	114	292	154	83	194	94	234	105	274	116	314	127	354	138	394	30
35	150	75	160	115	172	155	303	195	314	235	325	275	336	315	8	355	19	395	370
36	31	76	41	116	53	156	183	196	194	236	205	276	216	316	348	356	359	396	250
37	371	77	381	117	393	157	64	197	75	237	86	277	97	317	228	357	239	397	130
38	251	78	261	118	273	158	284	198	295	238	306	278	317	318	109	358	119	398	11
39	131	79	141	119	153	159	164	199	175	239	186	279	197	319	329	359	339	399	351
40	12	80	22	120	34	160	45	200	56	240	67	280	78	320	209	360	219	400	231

Natural Science Foundation of Hunan Province (No. 2022JJ20012), and the Science and Technology Innovation Program of Hunan Province (No. 2022RC1176), and the China Scholarship Council (CSC) for this research.

Appendix. The values of new generating vector v for $n_t = 400$.

The value of the new generating vector **v** for $n_t = 400$ calculated by the proposed method are listed in Table A.6.

Data availability

Data will be made available on request.

References

[1] Navaneeth N, Chakraborty S. Surrogate assisted active subspace and active subspace assisted surrogate—a new paradigm for high dimensional structural reliability analysis. Comput Methods Appl Mech Engrg 2022;389:114374.

[2] Haldar A, Mahadevan S. Reliability assessment using stochastic finite element analysis. John Wiley & Sons; 2000.

[3] Alibrandi U, Mosalam KM. Distributions with independent components for uncertainty quantification and structural reliability analysis. In: Proceedings of the 13th international conference on applications of statistics and probability in civil engineering. 2019, p. 26–30.

[4] Wang Z, Song J. Cross-entropy-based adaptive importance sampling using von mises-fisher mixture for high dimensional reliability analysis. Struct Saf 2016;59:42–52.

[5] Keshtegar B, Meng Z. A hybrid relaxed first-order reliability method for efficient structural reliability analysis. Struct Saf 2017;66:84–93.

[6] Li G, Li B, Hu H. A novel first–order reliability method based on performance measure approach for highly nonlinear problems. Struct Multidiscip Optim 2018;57:1593–610.

[7] Lee I, Noh Y, Yoo D. A novel second-order reliability method (SORM) using noncentral or generalized chi-squared distributions. J Mech Des 2012;134(10):100912.

[8] Huang X, Li Y, Zhang Y, Zhang X. A new direct second-order reliability analysis method. Appl Math Model 2018;55:68–80.

[9] Ditlevsen O, Madsen HO. Structural reliability methods, vol. 178, New York: Wiley; 1996.

[10] Meng Z, Zhou H. New target performance approach for a super parametric convex model of non-probabilistic reliability-based design optimization. Comput Methods Appl Mech Engrg 2018;339:644–62.

[11] Dang C, Xu J. Unified reliability assessment for problems with low-to high-dimensional random inputs using the laplace transform and a mixture distribution. Reliab Eng Syst Saf 2020;204:107124.

[12] Valdebenito M, Pradlwarter H, Schuëller G. The role of the design point for calculating failure probabilities in view of dimensionality and structural nonlinearities. Struct Saf 2010;32(2):101–11.

[13] Dang C, Faes MG, Valdebenito MA, Wei P, Beer M. Partially bayesian active learning cubature for structural reliability analysis with extremely small failure probabilities. Comput Methods Appl Mech Engrg 2024;422:116828.

[14] He W, Wang Y, Li G, Zhou J. A novel maximum entropy method based on the b-spline theory and the low-discrepancy sequence for complex probability distribution reconstruction. Reliab Eng Syst Saf 2023;109909.

[15] Tabandeh A, Jia G, Gardoni P. A review and assessment of importance sampling methods for reliability analysis. Struct Saf 2022;97:102216.

[16] Zhang X, Lu Z, Cheng K. Cross-entropy-based directional importance sampling with von mises-fisher mixture model for reliability analysis. Reliab Eng Syst Saf 2022;220:108306.

[17] Geyer S, Papaioannou I, Straub D. Cross entropy-based importance sampling using gaussian densities revisited. Struct Saf 2019;76:15–27.

[18] Papaioannou I, Papadimitriou C, Straub D. Sequential importance sampling for structural reliability analysis. Struct Saf 2016;62:66–75.
[19] Cheng K, Papaioannou I, Lu Z, Zhang X, Wang Y. Rare event estimation with sequential directional importance sampling. Struct Saf 2023;100:102291.
[20] Au S-K, Beck JL. Estimation of small failure probabilities in high dimensions by subset simulation. Probab Eng Mech 2001;16(4):263–77.
[21] Cheng K, Lu Z, Xiao S, Lei J. Estimation of small failure probability using generalized subset simulation. Mech Syst Signal Process 2022;163:108114.
[22] Koutsourelakis P, Pradlwarter H, Schuëller G. Reliability of structures in high dimensions, Part I: algorithms and applications. Probabilistic Eng Mech 2004;19(4):409–17.
[23] Koutsourelakis P. Reliability of structures in high dimensions, Part II. theoretical validation. Probabilistic Eng Mech 2004;19(4):419–23.
[24] Xu J, Dang C. A novel fractional moments-based maximum entropy method for high-dimensional reliability analysis. Appl Math Model 2019;75:749–68.
[25] Zhou T, Peng Y. Kernel principal component analysis-based gaussian process regression modelling for high-dimensional reliability analysis. Comput Struct 2020;241:106358.
[26] Wang L, Hu Z, Dang C, Beer M. Refined parallel adaptive bayesian quadrature for estimating small failure probabilities. Reliab Eng Syst Saf 2024;244:109953.
[27] Faravelli L. Response-surface approach for reliability analysis. J Eng Mech 1989;115(12):2763–81.
[28] Hadidi A, Azar BF, Rafiee A. Efficient response surface method for high-dimensional structural reliability analysis. Struct Saf 2017;68:15–27.
[29] Ghosh S, Roy A, Chakraborty S. Support vector regression based metamodeling for seismic reliability analysis of structures. Appl Math Model 2018;64:584–602.
[30] Cheng K, Lu Z. Adaptive bayesian support vector regression model for structural reliability analysis. Reliab Eng Syst Saf 2021;206:107286.
[31] Echard B, Gayton N, Lemaire M. Ak-mcs: An active learning reliability method combining kriging and monte carlo simulation. Struct Saf 2011;33(2):145–54.
[32] Zhao Z, Lu Z-H, Zhao Y-G. An efficient extreme value moment method combining adaptive kriging model for time-variant imprecise reliability analysis. Mech Syst Signal Process 2022;171:108905.
[33] Zhou J, Li J. Ie-ak: A novel adaptive sampling strategy based on information entropy for kriging in metamodel-based reliability analysis. Reliab Eng Syst Saf 2023;229:108824.
[34] Cheng J, Li Q. Reliability analysis of structures using artificial neural network based genetic algorithms. Comput Methods Appl Mech Engrg 2008;197(45):3742–50.
[35] Chakraborty S. Transfer learning based multi-fidelity physics informed deep neural network. J Comput Phys 2021;426:109942.
[36] Sudret B. Global sensitivity analysis using polynomial chaos expansions. Reliab Eng Syst Saf 2008;93(7):964–79.
[37] Xu J, Kong F. A cubature collocation based sparse polynomial chaos expansion for efficient structural reliability analysis. Struct Saf 2018;74:24–31.
[38] Ni P, Li J, Hao H. Reliability analysis of bridges under different loads using polynomial chaos and subset simulation. Earthq Eng Resil 2023;2(2):163–79.
[39] Rahman S. Uncertainty quantification under dependent random variables by a generalized polynomial dimensional decomposition. Comput Methods Appl Mech Engrg 2019;344:910–37.
[40] Wang T, Chen Z, Li G, He J, Liu C, Du X. A novel method for high-dimensional reliability analysis based on activity score and adaptive kriging. Reliab Eng Syst Saf 2024;241:109643.
[41] Wang J, Xu G, Yuan P, Li Y, Kareem A. An efficient and versatile kriging-based active learning method for structural reliability analysis. Reliab Eng Syst Saf 2024;241:109670.
[42] Pan Q, Dias D. Sliced inverse regression-based sparse polynomial chaos expansions for reliability analysis in high dimensions. Reliab Eng Syst Saf 2017;167:484–93, special Section: Applications of Probabilistic Graphical Models in Dependability, Diagnosis and Prognosis.
[43] Lataniotis C, Marelli S, Sudret B. Extending classical surrogate modeling to high dimensions through supervised dimensionality reduction: a data-driven approach. Int J Uncertain Quantif 2020;10(1).
[44] Zhou T, Peng Y. Structural reliability analysis via dimension reduction, adaptive sampling, and monte carlo simulation. Struct Multidiscip Optim 2020;62(5):2629–51.
[45] Xu J, Zhang Y, Dang C. A novel hybrid cubature formula with pearson system for efficient moment-based uncertainty propagation analysis. Mech Syst Signal Process 2020;140:106661.
[46] Liu J, Meng X, Xu C, Zhang D, Jiang C. Forward and inverse structural uncertainty propagations under stochastic variables with arbitrary probability distributions. Comput Methods Appl Mech Engrg 2018;342:287–320.
[47] Xu J, Dang C, Kong F. Efficient reliability analysis of structures with the rotational quasi-symmetric point-and the maximum entropy methods. Mech Syst Signal Process 2017;95:58–76.
[48] Mead LR, Papanicolaou N. Maximum entropy in the problem of moments. J Math Phys 1984;25(8):2404–17.
[49] Ormoneit D, White H. An efficient algorithm to compute maximum entropy densities. Econometric Rev 1999;18(2):127–40.
[50] Zhang X, Pandey MD. Structural reliability analysis based on the concepts of entropy, fractional moment and dimensional reduction method. Struct Saf 2013;43:28–40.
[51] Zhang X, Wang X, Pandey MD, Sørensen JD. An effective approach for high-dimensional reliability analysis of train-bridge vibration systems via the fractional moment. Mech Syst Signal Process 2021;151:107344.
[52] Xu J, Kong F. Adaptive scaled unscented transformation for highly efficient structural reliability analysis by maximum entropy method. Struct Saf 2019;76:123–34.
[53] He S, Xu J, Zhang Y. Reliability computation via a transformed mixed-degree cubature rule and maximum entropy. Appl Math Model 2022;104:122–39.
[54] Li G, Wanxin H, Zeng Y. An improved maximum entropy method via fractional moments with laplace transform for reliability analysis. Struct Multidiscip Optim 2019;59:1301–20.
[55] Hua LK, Wang Y. Applications of number theory to numerical analysis. Berlin Heidelberg: Springer; 1972.
[56] Xu J, Wang D. A two-step methodology to apply low-discrepancy sequences in reliability assessment of structural dynamic systems. Struct Multidiscip Optim 2018;57:1643–62.
[57] Fang K, Wang Y. Number-theoretic methods in statistics, vol. 51, CRC Press; 1993.
[58] Korobov N. The approximate computation of multiple integrals. Dokl Akad Nauk Sssr 1959;(4):3–18.
[59] Qi Z-F, Zhang X-R, Zhou Y-D. Generalized good lattice point sets. Comput Statist 2018;33(2):887–901.
[60] Gao K, Liu G, Tang W. High-dimensional reliability analysis based on the improved number-theoretical method. Appl Math Model 2022;107:151–64.
[61] Niederreiter H. Existence of good lattice points in the sense of hlawka. Monatshefte Math 1978;86(3):203–19.
[62] Zhang Y, Xu J. A partial decomposition cutting method with cf-discrepancy for points selection in stochastic seismic analysis of structures. Struct Saf 2024;111:102513.
[63] Li H, Lü Z, Yuan X. Nataf transformation based point estimate method. Chin Sci Bull 2008;53(17):2586–92.
[64] Box GEP, Cox DR. An analysis of transformations. J R Stat Soc Ser B Stat Methodol 1964;26:211–43.
[65] Cai CH, Lu ZH, Zhao YG. Moment method with box–cox transformation for structural reliability. J Eng Mech 2020;146:04020086.
[66] Novi Inverardi PL, Tagliani A. Maximum entropy density estimation from fractional moments. Comm Statist Theory Methods 2003;32(2):327–45.
[67] Xu J, Dang C, Kong F. Efficient reliability analysis of structures with the rotational quasi-symmetric point- and the maximum entropy methods. Mech Syst Signal Process 2017;95:58–76.
[68] Gzyl H, Novi Inverardi P, Tagliani A. Entropy and density approximation from laplace transforms. Appl Math Comput 2015;265:225–36.
[69] Xu J, Zhu S. An efficient approach for high-dimensional structural reliability analysis. Mech Syst Signal Process 2019;122:152–70.
[70] Marelli S, Sudret B. Uqlab: A framework for uncertainty quantification in matlab. In: Proc. 2nd Int. Conf. on Vulnerability, uncertainty, and risk: quantification, mitigation, and management. 2014, p. 2554–63.